AGU PUBLICATIONS

Geochemistry, Geophysics, Geosystems

RESEARCH ARTICLE
10.1002/2015GC006010

Key Points:
- Atlantis II muds are chemical-clastic sediments with distinctive fine layering that is mainly diagenetic in origin
- Fe-(oxy)hydroxides, hydrothermal carbonates, sulfides, and authigenic clays are the main "ore" minerals
- Sequential leaching indicates nanophase hematite and nonsulfidic compounds are important components

Supporting Information:
- Supporting Information S1

Correspondence to:
M. D. Hannington,
mhannington@geomar.de

Citation:
Laurila, T. E., M. D. Hannington, M. Leybourne, S. Petersen, C. W. Devey, and D. Garbe-Schönberg (2015), New insights into the mineralogy of the Atlantis II Deep metalliferous sediments, Red Sea, *Geochem. Geophys. Geosyst.*, *16*, 4449–4478, doi:10.1002/2015GC006010.

Received 13 JUL 2015
Accepted 5 DEC 2015
Accepted article online 14 DEC 2015
Published online 31 DEC 2015

New insights into the mineralogy of the Atlantis II Deep metalliferous sediments, Red Sea

Tea E. Laurila[1,2], Mark D. Hannington[1,2], Matthew Leybourne[3], Sven Petersen[1], Colin W. Devey[1], and Dieter Garbe-Schönberg[4]

[1]GEOMAR, Helmholtz Centre for Ocean Research Kiel, Kiel, Germany, [2]Department of Earth and Environmental Sciences, University of Ottawa, Ontario, Canada, [3]Department of Earth Sciences, Laurentian University, Sudbury, Ontario, Canada, [4]Institute of Geosciences, Christian-Albrechts-Universität zu Kiel, Kiel, Germany

Abstract The Atlantis II Deep of the Red Sea hosts the largest known hydrothermal ore deposit on the ocean floor and the only modern analog of brine pool-type metal deposition. The deposit consists mainly of chemical-clastic sediments with input from basin-scale hydrothermal and detrital sources. A characteristic feature is the millimeter-scale layering of the sediments, which bears a strong resemblance to banded iron formation (BIF). Quantitative assessment of the mineralogy based on relogging of archived cores, detailed petrography, and sequential leaching experiments shows that Fe-(oxy)hydroxides, hydrothermal carbonates, sulfides, and authigenic clays are the main "ore" minerals. Mn-oxides were mainly deposited when the brine pool was more oxidized than it is today, but detailed logging shows that Fe-deposition and Mn-deposition also alternated at the scale of individual laminae, reflecting short-term fluctuations in the Lower Brine. Previous studies underestimated the importance of nonsulfide metal-bearing components, which formed by metal adsorption onto poorly crystalline Si-Fe-OOH particles. During diagenesis, the crystallinity of all phases increased, and the fine layering of the sediment was enhanced. Within a few meters of burial (corresponding to a few thousand years of deposition), biogenic (Ca)-carbonate was dissolved, manganosiderite formed, and metals originally in poorly crystalline phases or in pore water were incorporated into diagenetic sulfides, clays, and Fe-oxides. Permeable layers with abundant radiolarian tests were the focus for late-stage hydrothermal alteration and replacement, including deposition of amorphous silica and enrichment in elements such as Ba and Au.

1. Introduction

The Atlantis II Deep was one of the first recognized locations of metal deposition associated with seafloor hydrothermal activity [e.g., *Miller*, 1964; *Miller et al*., 1966; *Degens and Ross*, 1969]. The Deep is situated in the slowly spreading Red Sea rift axis at a water depth of 2.2 km (Figure 1) and contains a major ore deposit composed of highly metalliferous muds [~90 Mt at 2% Zn, 0.5% Cu, 40 g/t Ag, and 0.5 g/t Au dry weight, salt free) [*Nawab*, 1984; *Guney et al*., 1988]. The deposit consists of ~20 m of fine-grained, laminated sediments, composed of oxides, sulfides, silicates, and carbonates, that cover an area of about 60 km^2. A stratified brine pool occupies the bottom of the Deep and overlies the entire deposit (Figure 2). The Lower Brine is 135 m thick at the deepest part of the basin and has a volume of ~4 km^3. It is anoxic, extremely saline (~27 wt % NaCl), hot (~68°C in 2008) [*Swift et al*., 2012], and devoid of reduced sulfur [*Anschutz et al*., 1998]. The Upper Brine is ~50 m thick and progressively more seawater-like with height above the Lower Brine [*Swift et al*., 2012].

The style of metal accumulation in the Atlantis II Deep is not known anywhere else on the modern seafloor but has been widely suggested as an analog for many ancient sediment-hosted ore deposits [e.g., *Solomon et al*., 2004; *Goodfellow and Lydon*, 2007; *Tornos et al*., 2008]. In contrast to mid-ocean ridge (MOR) hydrothermal systems, where most of the metals are dispersed to the open ocean by buoyant hydrothermal plumes [*Baker et al*., 1985], metals in the Atlantis II Deep have been effectively trapped by the brine pool [*Bignell et al*., 1976; *Gurvich*, 2006]. Hydrothermal venting was initially located in the northeast part of the basin about 15,000 years ago [*Shanks and Bischoff*, 1980] but has since shifted to the Southwest Basin (referred to as "vent proximal" in Figure 1). Proximity to hydrothermal venting is recognized by the higher metal grades and presence of anhydrite veining in the muds. During periods of enhanced hydrothermal

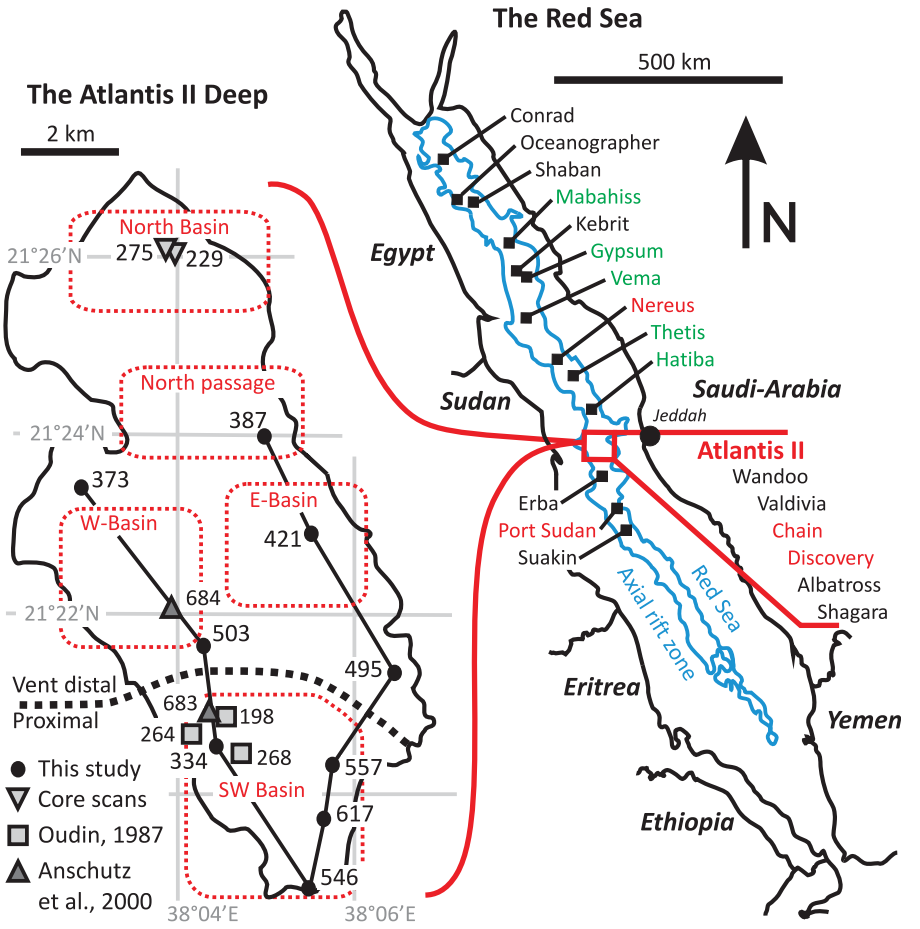

Figure 1. Location of the Atlantis II Deep and other brine-filled basins of the Red Sea. Deeps with hot brines are indicated by the red font; basins with cold brines are indicated in green font. The subbasins and core locations in the Atlantis II Deep are shown on the left. The proximal and distal parts of the Deep with respect to the currently active venting in the SW Basin are delineated approximately by Zn concentrations of >2.5 wt % (bulk core, salt free, based on unpublished data on 497 cores from the MESEDA I-III projects) [*Bertram et al.*, 2011]. The lower stratigraphic units are missing in the SW Basin.

venting, abundant Fe-(oxy)hydroxides precipitated in the brine pool at the interface between the Lower Brine and the more oxidized Upper Brine (Figure 2). The metalliferous sediment accumulated by settling of these particles from the brine pool [*Shanks and Bischoff*, 1977, 1980], which is continuing today. Mn-(oxy)-hydroxides precipitate only within the Upper Brine layers, where oxygen is available, and today are deposited mainly on the flanks of the Deep. However, during times of diminished hydrothermal activity and more oxidized Lower Brine, Mn-(oxy)hydroxides also have been deposited at the bottom of the Deep [*Butuzova et al.*, 1990; *Blanc et al.*, 1998]. Sulfide precipitation, in particular Zn-sulfide, has occurred close to the seafloor near the vent location(s) at temperatures reaching ~100–200°C [*Shanks and Bischoff*, 1977; *Pottorf and Barnes*, 1983; *Cole*, 1988], whereas Cu-sulfides were precipitated mainly below the brine-sediment interface due to cooling of deeper hydrothermal fluids from ~350°C [*Zierenberg and Shanks*, 1983; *Oudin et al.*, 1984; *Ramboz et al.*, 1988; *Missack et al.*, 1989]. Sulfides also have been found in a particle plume produced by hydrothermal fluid vented into the Lower Brine [*Hartmann*, 1973, 1985; *Schoell*, 1976]. Although the Lower Brine is highly enriched in metals, it is devoid of reduced sulfur, and so sulfide deposition is largely restricted to the vent proximity [*Brewer and Spencer*, 1969; *Shanks and Bischoff*, 1977; *Anschutz et al.*, 2000].

Previous studies of the mineralogy of the sediments focused on vent-proximal cores. Early descriptions also aimed to characterize only the major stratigraphic units that are on the order of several meters to tens of meters in thickness [*Bischoff*, 1969; *Bäcker and Richter*, 1973; *Blanc et al.*, 1998]. Different layers within those units were usually grouped together, complicating efforts to identify the controls on metal deposition. The precise mineralogy was often difficult to identify because of the small grain sizes (60% <2 μm) [*Bäcker and*

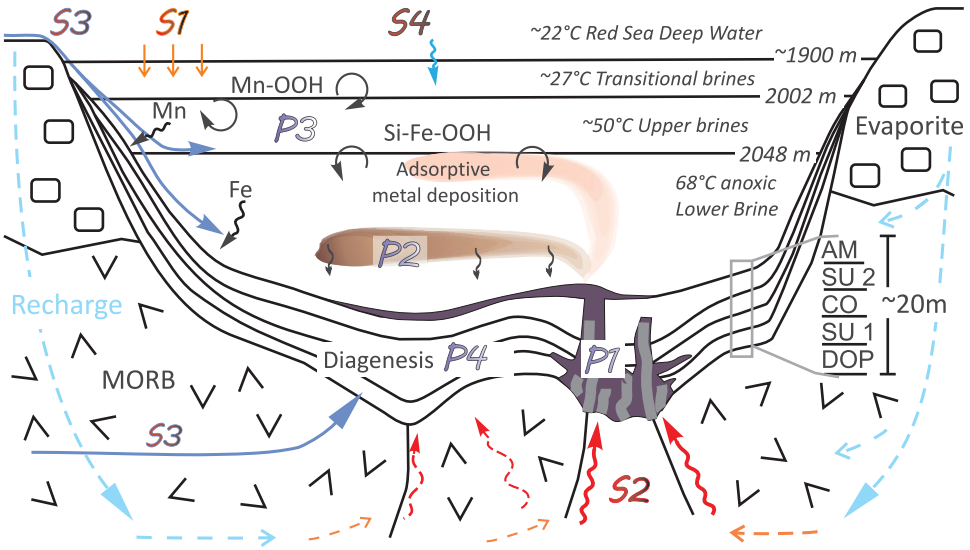

Figure 2. Schematic cross section of the Atlantis II Deep sediments and brine pool. The present thickness of the sedimentary strata is about 20 m, and the sediments are overlain by 150–180 m of stratified brine. The brine pool consists of a lower anoxic layer (Lower Brine) and an Upper Brine which comprises a number of sublayers that are progressively more seawater-like with height above the Lower Brine (modified after *Zierenberg and Shanks* [1988] and *Swift et al*. [2012]). Metals and other elements in the basin have four main sources [cf. *Laurila et al*., 2014b]: (S1) background sedimentation that brings biogenic pelagic and detrital silicic particles into the Deep; (S2) hot hydrothermal brines formed by seawater circulation through evaporites and underlying basalts; (S3) cold, bottom-hugging brines that have reacted with the surrounding sediments (evaporites and shales) before entering the Deep; and (S4) Red Sea deep water. Elements from seawater are brought into the Deep via redox driven Mn-(oxy)hydroxide and Fe-(oxy)hydroxide precipitation-dissolution cycling at the chemoclines. By far, most of the metals in the brine and sediment are derived from hot hydrothermal fluids, and they are incorporated in the sediments by four different pathways: (P1) precipitation of sulfides in high-temperature upflow zones; (P2) as sulfidic plume fall-out; (P3) adsorbed onto surface-active Si-Fe-(oxy)hydroxide particles that settle through the metal-rich Lower Brine; and (P4) incorporated in sulfides and nonsulfide minerals during diagenesis.

Richter, 1973], abundant amorphous material, and the finely laminated character of the sediments. Many samples used for mineralogical studies were also washed with distilled water to remove salt, so very fine-grained and water-soluble phases were lost [e.g., *Bischoff*, 1969; *Weber-Diefenbach*, 1977; *Shanks and Bischoff*, 1980; *Butuzova*, 1984]. In this paper, we present the first modern look at the very fine layering of the sediments, including relogging of selected cores, high-resolution petrography and elemental analysis, and sequential leaching experiments. The results offer new insight into the primary mineralogy, the formation of Fe-minerals and Mn-minerals, the fate of surface-active particles following deposition, and the effects of diagenesis and hydrothermal alteration on the fine layering and the distribution of "ore" metals.

2. Sediment Stratigraphy

The stratigraphy of the Atlantis II sediments was defined by *Bäcker and Richter* [1973], who distinguished five units based on 78 cores (Figure 3 and supporting information Table S1). The different units reflect changes in the intensity and location of hydrothermal activity within the Deep over thousands of years. The lowermost stratigraphic unit (detrital oxidic pyritic [DOP] unit) is composed mostly of siliciclastic and biogenic detrital material. Limonitic and manganitic layers and disseminated pyrite are present and become more abundant up stratigraphy, recording the change from normal marine to dominantly hydrothermal

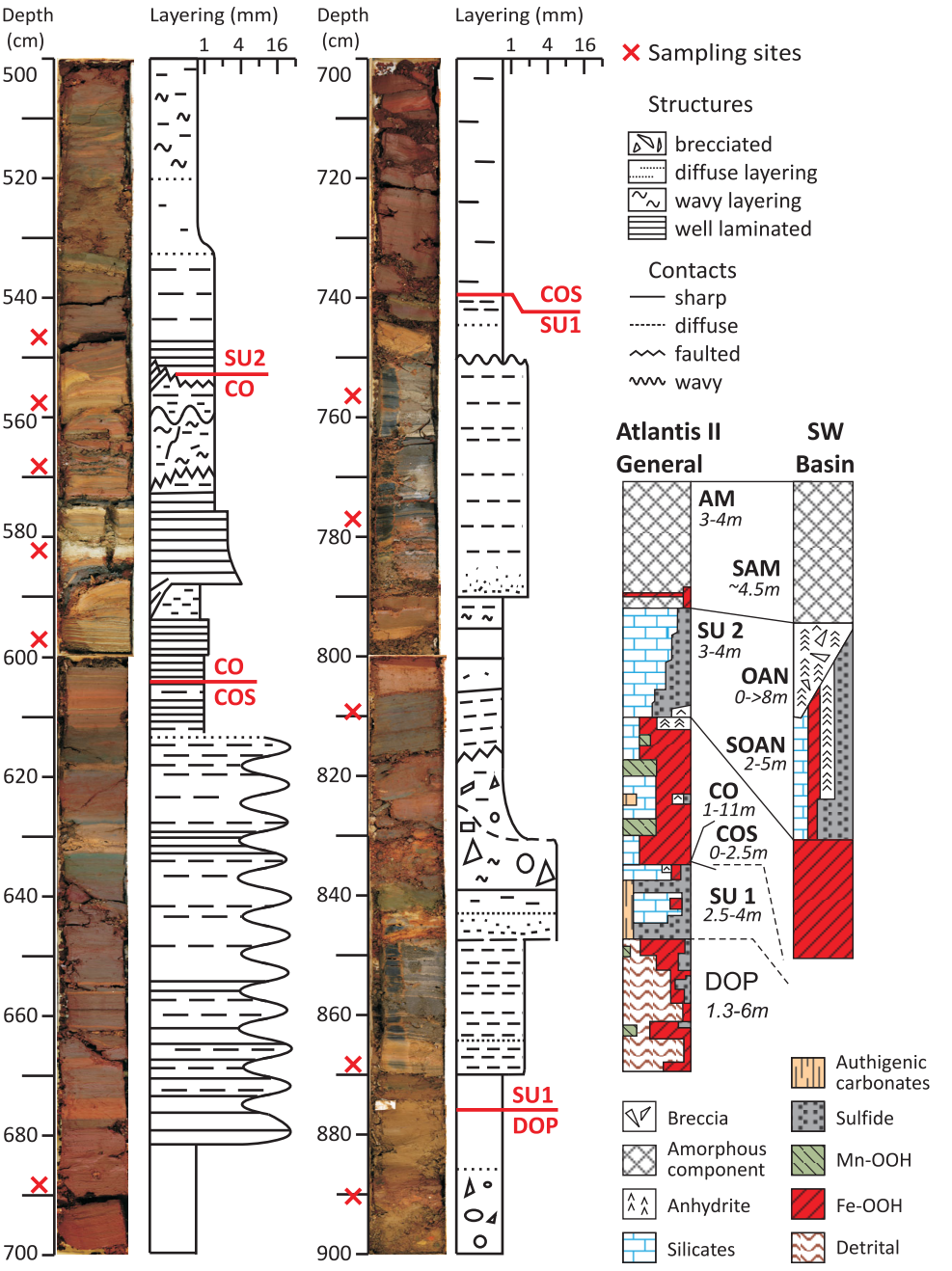

Figure 3. Example of a 4 m long core from the vent distal metalliferous sediment (core 495 at depth 5–9 m; cf. Figure 1 for location). The core includes sediment from unit DOP to SU2; the latter is compositionally gradational with the overlying AM unit, and laminations become more pronounced with depth in the core below SU2. On the right is a schematic illustration of the corresponding stratigraphy of the Atlantis II sediment based on 76 cores from *Bäcker and Richter* [1973]. The SAM, SOAN, and OAN units are found in the Southwest Basin, but the SU1 and DOP units are missing in the central part of the Southwest Basin due to the presence of a basaltic sill. The CO and COS units are found basin-wide. Samples referred to in the text are designated by core number and depth (e.g., sample 495-859 is from core 495 at a depth of 859 cm).

sedimentation [*Blanc et al.*, 1998]. The DOP unit is overlain by the first of two sulfidic units (SU1), which formed during the period when hydrothermal venting was located in the northeast part of the Deep. In the Southwest Basin, the DOP unit and SU1 are inaccessible due to the presence of a sill-like intrusion of basalt above SU1.

The sulfidic units contain abundant sulfides but also Fe-(oxy)hydroxides, Fe-bearing and Si-bearing clays (e.g., nontronite and montmorillonite), carbonates, and anhydrite [*Bischoff*, 1969; *Bäcker and Richter*, 1973;

Pottorf and Barnes, 1983]. The top of SU1 is marked by a sharp contact with the overlying central oxidic (CO) unit, which consists mainly of Mn-(oxy)hydroxides and Fe-(oxy)hydroxides, carbonates, and locally anhydrite. The formation of the CO unit recorded a time of intense tectonic activity marked by brecciation of the sediment (e.g., Figure 4a), during which the location of the vent source shifted from the northeast to its present location in the Southwest Basin [*Bäcker and Richter*, 1973; *Gurvich*, 2006]. The brine pool was also more oxidized at this time, as evidenced by precipitation of abundant Mn-oxides. Although Mn-(oxy)hydroxides and Fe-(oxy)hydroxides were deposited during the formation of the CO unit, little Cu, Zn, or sulfide minerals are found in the sediments, implying that the temperature of hydrothermal venting was lower than it is today. In the northeast part of the Deep, the CO unit contains abundant silicates (authigenic clays) and is referred to as the central oxidic siliceous (COS) unit.

The deposition of CO was terminated by the outbreak of higher-temperature hydrothermal activity in the Southwest Basin and is marked by the second sulfidic unit (SU2). Abundant Fe-(oxy)hydroxides and anhydrite at the base of SU2 gradually give way to Fe-carbonates and Mn-carbonates ($\pm$anhydrite) and finally to abundant sulfides up stratigraphy, similar to SU1. The ratio of Cu/Zn and total metals/sulfur in the sediment also increase upward [*Blanc et al*., 1998; *Laurila et al*., 2014a]. In the vent-proximal (southwest) part of the Deep, SU2 is subdivided into the oxidic anhydritic (OAN) and sulfidic oxidic anhydritic (SOAN) units (Figure 4c).

The topmost unit, referred to as the amorphous siliceous unit (AM), is composed mainly of poorly crystalline Si-Fe-(oxy)hydroxides, which represent the present-day metal deposition. In the vent-proximal part of the Deep, AM is locally referred to as the sulfidic amorphous siliceous (SAM) unit. The AM unit is saturated with brine (up to 95 wt %) and has a higher metal content than most of the other sediments [*Gurvich*, 2006]. The pore water is compositionally similar to the Lower Brine in terms of pH, Eh, and SO_4 concentration, but lower in carbonate and higher in metals [*Craig*, 1969; *Hendricks et al*., 1969; *Schoell and Stahl*, 1972; *Anschutz et al*., 2000]. *Blanc et al*. [1998] considered the AM unit to be a "precursor" or continuation of SU2 due to the high metal contents. However, it is separated from SU2, almost basin-wide, by a bright orange lepidocrocite horizon [*Bäcker and Richter*, 1973] (Figure 4b), which is interpreted to have formed when an oxidized, bottom-hugging brine sourced from evaporites exposed on the flanks entered the Deep [*Taitel-Goldman et al*., 2002]. Where the lepidocrocite horizon is absent, the transition between SU2 and AM is gradational.

3. Mineralogy and Bulk Composition of the Atlantis II Sediments: Previous Work

Previous studies defined a number of different facies within the stratigraphic units, according to the dominant mineralogy: Fe-smectite, goethite, sulfide, manganosiderite, anhydrite, and manganite [*Bischoff*, 1969; *Bäcker and Richter*, 1973; *Bäcker*, 1976] (see also Figure 3). However, the different facies are rarely monomineralic. The upper units contain 80–90 vol % authigenic components and 10–20 vol % normal deep-sea sediment of the Red Sea (deposited at a rate of $\sim$10 cm/1000 years) [*Ku et al*., 1969; *Stoffers and Ross*, 1974]. Fe-(oxy)hydroxides account for more than 50 vol % of the authigenic component; siliceous material consisting of Si-Fe-(oxy)hydroxides and clays accounts for $\sim$20 vol %, and hydrothermal carbonates and sulfides each account for $\sim$10 vol %. Sulfates, Mn-oxides, and other nonsulfidic metal-bearing minerals make up $<$10 vol % (supporting information Table S2).

The detrital input consists mainly of biogenic carbonates ($\sim$80 vol %), including aragonitic pteropod shells, calcitic foraminiferal tests, and coccoliths, with minor radiolarian silica tests [*Stoffers and Ross*, 1974] (e.g., Figure 4d). Terrigenous clastic material accounts for the remainder ($\sim$20 vol %) and includes mainly quartz, feldspar, and altered volcanic ash (montmorillonite, cristobalite, and devitrified volcanic glass) [*Stoffers and Ross*, 1974]. Biogenic detrital carbonate was thickly deposited at the beginning of hydrothermal activity, and this type of sediment dominates the DOP unit [*Anschutz and Blanc*, 1995a; *Blanc et al*., 1998]. However, calcite is soluble in the current Lower Brine [*Bischoff*, 1969; *Blanc et al*., 1998], and so carbonate detritus is much less abundant in the more metalliferous units ($<$10 vol %). Siliceous biogenic components are common, but the greatest influx of biogenic silica was restricted to a short period in the history of the Deep, $\sim$9000–12,000 years ago, when radiolaria from the Indian Ocean had brief access to the Red Sea due to globally high sea-level stands [*Goll*, 1969].

During episodes of high-temperature hydrothermal activity, the total sedimentation rate increased dramatically and is estimated to have been as high as $\sim$100–120 cm/1000 years [*Shanks and Bischoff*, 1980] or $\sim$1 mm annually. This corresponds closely to the thickness of many of the fine laminations in the most

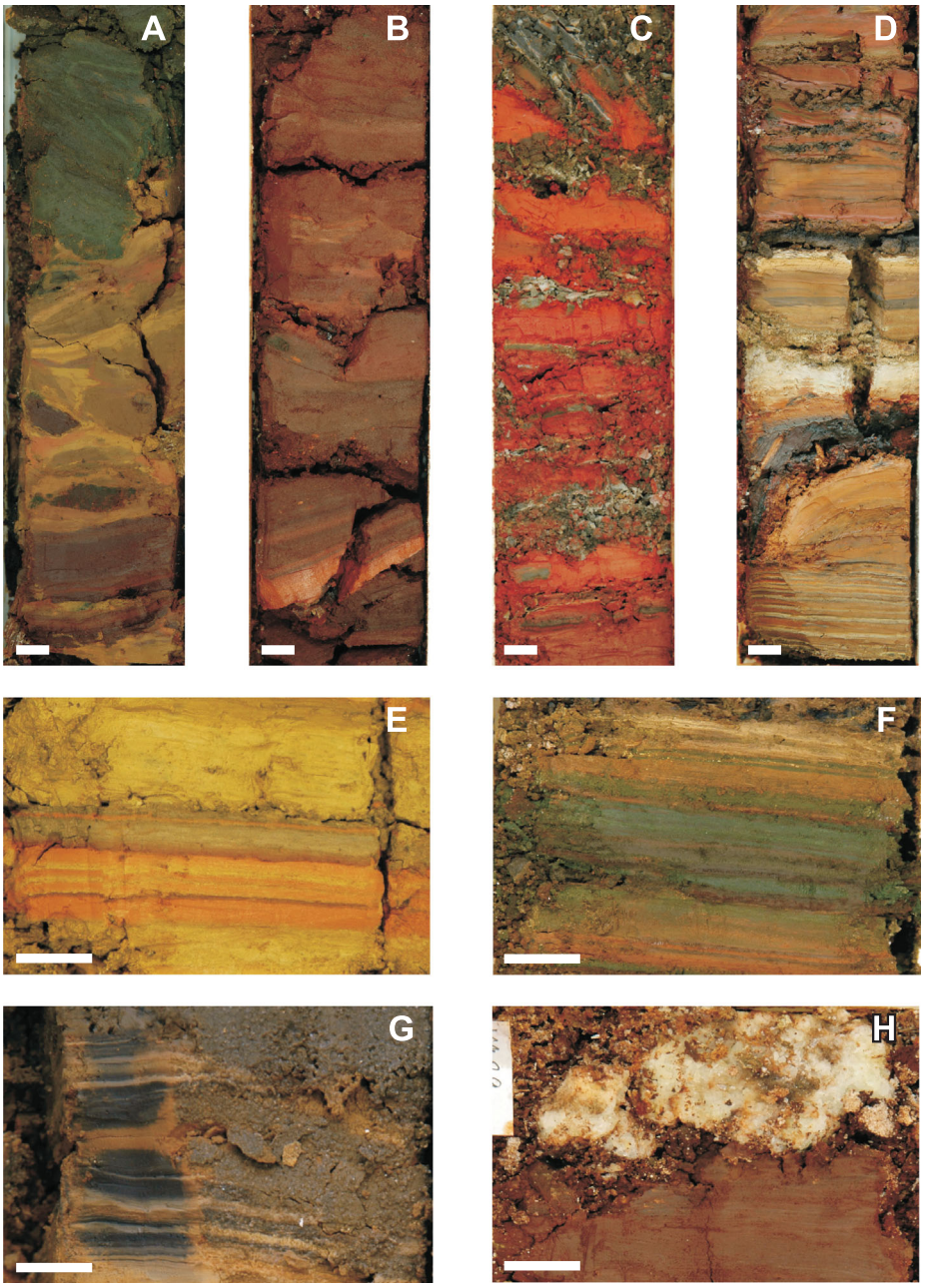

Figure 4. Photographs of typical Atlantis II metalliferous sediment, all scale bars are 2 cm. (a) An example of brecciated mud; the top part of the photograph consists mainly of clays (green), whereas the lower part is dominated by Fe-(oxy)hydroxides (from unit COS in core 373 at 460-500 cm). (b) Gradational and diffuse lamination typical of the upper strata. The orange band is the lepidocrocite horizon that separates SU2 from AM (core 373 at 10–50 cm). (c) Bright red Fe-(oxy)hydroxide and grey anhydrite-rich layers from a vent-proximal core 617 at 358–398 cm (unit OAN). The top part of The photograph shows subvertical veins of anhydrite. (d) Finely laminated sediment in unit CO composed mainly of Fe-(oxy)hydroxides interlayered with hydrothermal carbonates and Mn-(oxy)hydroxides. The dark grey layer, at an angle to the fine laminations, is composed mainly of Mn-(oxy)hydroxide. The white layer is composed of detrital silicates and biogenic calcite. The top part of the photograph shows alternating layers of Fe-(oxy)hydroxides (red) and Mn-(oxy)hydroxides (dark grey); from core 495 at depth 560–600 cm (detail from Figure 3). (e) Finely laminated Fe-(oxy)hydroxides in unit DOP (core 373 at 789–797 cm). The different colors are due to variations in the abundance of different minerals (esp. clays) mixed with the Fe-(oxy)hydroxides. The yellowish layers (top and bottom of photo) contain abundant detrital material, whereas brighter orange and red laminae have a higher proportion of Fe-(oxy)hydroxides. (f) Finely laminated section from unit DOP containing abundant authigenic clays (green layers; core 421 at 878–886 cm). Red, yellow, and brown laminae are dominated by Fe-(oxy)hydroxides with carbonates; light beige laminae are dominated by detrital components. Sharp contacts between laminae are typical of the lower stratigraphy, compared to the more diffuse laminations in the upper strata (shown in Figure 4b). (g) Interlayered sulfide (dark) and detrital sediment (light) in unit SU1 (core 495 at 858–866 cm; detail from Figure 3). The right-hand side of the core shows the effect of surface oxidation during core storage; this was removed on the left side of the core to reveal the well-preserved layering. (h) Layer of anhydrite in unit SU1 (core 387 at 500–507 cm) showing a sharp contact with the underlying sediment.

metal-rich sediment (e.g., Figures 4d–4f), although it is now clear that accumulation rates were not the only control on the fine layering. Fe-(oxy)hydroxides and authigenic clays were the dominant hydrothermal precipitates (e.g., brown and orange layers in Figures 4d and 4e and green layers in 4f). The primary precipitates are thought to have accumulated on the seafloor as a noncrystalline Si-Fe-OOH "gel," which is still forming in the AM unit today. They are thought to have been sourced mainly from the brine layers, as *Hartmann* [1973] found abundant particulate Fe-(oxy)hydroxides in the Lower Brine and especially at the contact with the Upper Brine. Although some of these very fine-grained minerals and other poorly crystalline compounds are preserved in the upper layers of sediment cores, most have been transformed into more crystalline Fe-oxides and clay minerals during diagenesis [*Butuzova et al*., 1990; *Taitel-Goldman and Singer*, 2002a,b]. In particular, ferrihydrite, goethite (±limonite), lepidocrocite, and variably crystalline hematite and magnetite have been described in the deeper sediments [*Bischoff*, 1969; *Knedler*, 1985; *Butuzova et al*., 1988, 1990; *Schwertmann et al*., 1998; R. J. Pottorf, Hydrothermal sediments of the Red Sea, Atlantis II deep- a model for massive sulfide-type ore deposits. Pennsylvania State University, unpublished data, 1980].

Mn-oxide minerals are mainly present in the CO unit (e.g., Figure 4d). Well-crystallized manganite is the most common, but groutite, todorokite, and the Zn-bearing woodruffite also have been noted [*Bischoff*, 1969]. Manganite has remained a metastable phase in the sediment [*Diem and Stumm*, 1984] and is still present in archived cores today. *Bischoff* [1969] suggested that some coarse-grained Mn-oxide layers formed by alteration of preexisting carbonate layers; however, *Bäcker and Richter* [1973] considered the coarser Mn-oxides to represent recrystallization during core storage.

The authigenic clays (or their precursors) formed both in the brine pool and in the pore waters of the sediment [*Zierenberg and Shanks*, 1983; *Butuzova*, 1984]. The most common clays belong to the smectite group, and these have been studied extensively [e.g., *Bischoff*, 1969, 1972; *Bäcker and Richter*, 1973; *Goulart*, 1976; *Cole*, 1983, 1988; *Cole and Shaw*, 1983a; *Badaut et al*., 1985; *Schwertmann et al*., 1998; *Taitel-Goldman and Singer*, 2002b]. They include both Fe-rich and Si-rich end-members, but the few published analyses indicate that the dominant phase is saponite. The clays are more Mg rich at depth and in vent-proximal sediments and become more iron rich with distance away from the vents (approaching end-member nontronite) [*Zierenberg and Shanks*, 1983, 1988; *Singer and Stoffers*, 1987]. Most early workers recognized the highly variable crystallinity of the clays [e.g., *Badaut et al*., 1985], and more recently it has been suggested that the majority formed during diagenesis rather than by primary precipitation in the brine pool [*Badaut et al*., 1985, 1992; *Taitel-Goldman and Singer*, 2001, 2002a; *Taitel-Goldman et al*., 2004]. This is supported by a sharp decrease in pore fluid Si with burial [*Anschutz and Blanc*, 1995b], which is interpreted to reflect clay mineral formation from the initially deposited amorphous Si-Fe-OOH.

Other fine-grained aluminosilicates have been identified in trace amounts, including vermiculite [*Singer and Stoffers*, 1981], kerolite [*Cole and Shaw*, 1983b], talc, chlorite [*Zierenberg and Shanks*, 1983], and ferripyrophyllite-like minerals [*Badaut et al*., 1992] (supporting information Table S2). Some are associated with high-temperature venting, i.e., in subvertical veins of anhydrite, including chlorite, amphibole, pyroxene, garnet, and sphene [*Hackett and Bischoff*, 1973; *Cole and Shaw*, 1983b; *Zierenberg and Shanks*, 1983]. The calc-silicates are thought to have formed by contact metamorphism caused by intrusion of the basaltic sill in the Southwest Basin. Heating of the sediments, either by diffusive upflow of hydrothermal fluids or intrusion of basalt, also affected the Fe mineralogy, resulting in local transformation of hematite to magnetite [*Zierenberg and Shanks*, 1983].

Authigenic carbonates occur in all of the sediments and are locally quite abundant [*Blanc et al*., 1998]. They are mainly solid solutions between rhodocrosite and siderite, including ankerite and kutnohorite ("manganosiderite" facies of *Bischoff* [1969] and *Bäcker and Richter* [1973]). Dolomite is less common, although many of the carbonates contain minor Mg [*Bischoff*, 1969; *Blanc et al*., 1998]. Zn-bearing and Cu-bearing carbonates also have been described by *Oudin et al*. [1984], *Butuzova* [1984], and *Gurvich* [2006]. Hydrothermal or authigenic carbonates are distinguished from biogenic carbonates by the lack of clear fossil texture and because most biogenic carbonates are calcite rather than dolomite or Fe-bearing carbonate. A number of different pathways of formation of Fe-Mn carbonates have been suggested, including replacement of biogenic carbonate [*Bischoff*, 1969] and autocatalytic or bacterial reduction of Fe-oxides and Mn-oxides [*Blanc et al*., 1998].

Pyrite and sphalerite are the dominant sulfide minerals in the Atlantis II sediments and mainly occur as fine disseminations (50–80% <2 μm) in a matrix of Fe-(oxy)hydroxides, clays, carbonates, anhydrite, and other

authigenic phases. In the topmost sediments of the AM unit, where there is a very high interstitial brine content (down to about 1 m), the sulfides are mainly X-ray amorphous [*Hartmann*, 1973; *Brockamp et al*., 1978], consistent with early suggestions that the well-crystallized sulfide minerals in the cores formed during burial [*Weber-Diefenbach*, 1977; *Butuzova*, 1984]. Coarser grains of sulfides, a few tens of micrometers up to a few hundred micrometers, are common in or near the anhydrite veins, and they have textures suggesting precipitation directly from the cooling hydrothermal fluids [*Pottorf and Barnes*, 1983; *Missack et al*., 1989]. Black sulfidic layers in the sediment are the main record of increased hydrothermal activity in the Deep and are mainly found in SU1 and SU2 (e.g., Figure 4g). Sphalerite is dominant and is commonly found rimming chalcopyrite [e.g., *Pottorf and Barnes*, 1983], suggesting formation during waning stages of high-temperature hydrothermal activity, although the opposite also has been found [*Stephens and Wittkopp*, 1969]. Other Cu-sulfides include intermediate solid solution (ISS or cubic cubanite), isocubanite, covellite, chalcocite, digenite, and djurleite [*Pottorf and Barnes*, 1983]. Pyrrhotite is found in sediments closest to the hydrothermal vents, and the presence of other iron monosulfide(s), including amorphous FeS, mackinawite, and greigite, has been inferred from rapid reaction in cold HF [*Pottorf and Barnes*, 1983]. Pyrite occurs as framboids, spongy yellow pyrite, and as euhedral grains. The framboidal pyrite is abundant in the lowermost units and distal to the currently known vent sources [*Sweeney and Kaplan*, 1973; *Pottorf and Barnes*, 1983]. Marcasite has been found rarely.

Anhydrite, barite, gypsum, and bassanite are present in many sediment cores [*Zierenberg and Shanks*, 1983; *Blanc et al*., 1998] (e.g., Figures 4c and 4h). The gypsum and basanite likely formed after core recovery, as these minerals would not have been stable in the brines. Anhydrite is most abundant in sediments close to areas of hydrothermal venting, as veins and as massive beds, some up to several meters thick [*Bäcker and Richter*, 1973; *Zierenberg and Shanks*, 1983]. The veins, which locally contain abundant sulfides, have been studied extensively by *Zierenberg and Shanks* [1983], *Oudin et al*. [1984], and *Ramboz et al*. [1988]. The more massive beds of anhydrite are part of laterally extensive sill-like bodies, hundreds of meters in strike length, that are interpreted to have formed in response to magmatic heating of brine in the sediments [*Shanks and Bischoff*, 1977]. Barite is undersaturated in the Lower Brine [*Shanks and Bischoff*, 1977] but is found in crusts on the flanks of the basin [e.g., *Sval'nov et al*., 1984].

4. Sampling and Methodology

An extensive archive of Red Sea cores has been maintained at GEOMAR since the early studies of the Atlantis II Deep. We selected one hundred samples from nine brine-saturated sediment cores collected during the *R/V Valdivia* cruise 29 in 1980 (Figure 1). After recovery, the cores were split, and one half was sealed and stored in a cool warehouse. The selected cores were 5–12 m long and contained all five lithostratigraphic units. When reopened for this study, the sediments were in excellent condition and still moist, although the cut surfaces were encrusted with salt and had a thin layer of surface oxidation. When the crystalline salt and surface oxidation were removed, the delicate layering of the sediments could be readily logged and sampled. To obtain a more precise image of the internal layering of the units, two representative cores from the northern part of the Deep, where the sections are most condensed, were scanned using an automated energy-dispersive X-ray fluorescence scanner (AVAATEC Scanner) at the University of Kiel. Intensities of X-rays for different elements were measured on untreated surfaces of the cores at 2 mm intervals with count times of 10 s (Figure 5).

After relogging all nine cores, samples were taken with a 2 cm diameter minicore or by cutting the sediment from the core box with a spatula. This approach, which aimed to collect discrete layers, contrasts with most previous studies based on composite samples of several tens of centimeters up to 1 m in length [e.g., *Hendricks et al*., 1969; *Bäcker and Richter*, 1973; *Shanks and Bischoff*, 1980; *Gurvich*, 2006]. The minicores were dried at 40°C, during which pore water was evaporated. However, the sediments were not washed, thus preserving water-soluble compounds and other phases that would have passed the filters used during washing in previous studies. The mineralogy of the samples was determined by a combination of petrographic examination, X-ray diffraction (XRD), and electron microbeam techniques. XRD analyses were carried out at the University of Ottawa on a PANanalytical XRD system, using Phillips' XPert system software to identify the minerals. Polished thin sections of the samples were also prepared from the undisturbed sediment; 2 × 3 cm blocks cut from the minicores were dried in air and impregnated with epoxy to preserve

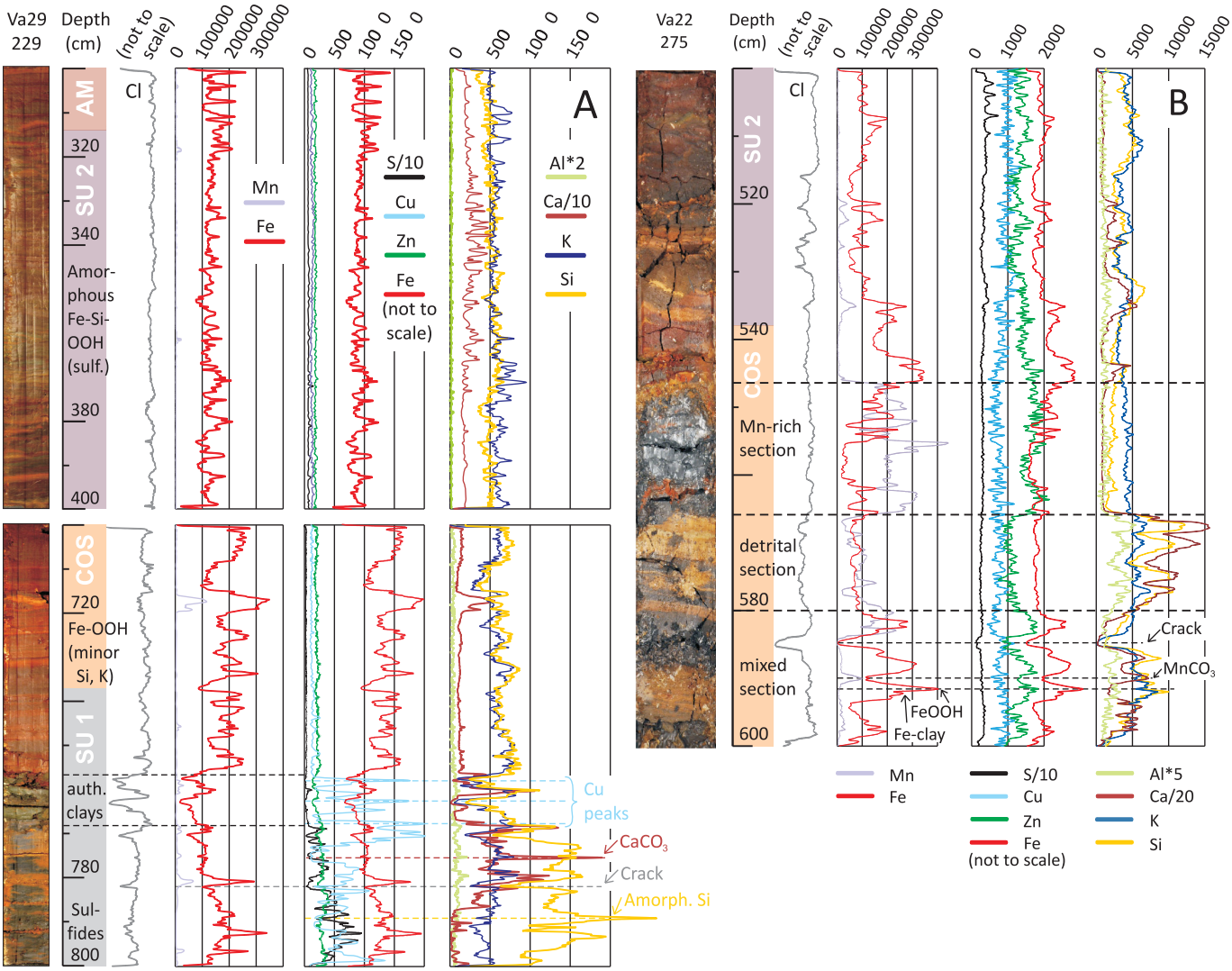

Figure 5. Representative XRF core scans of two cores from the northern part of the Atlantis II Deep (core Va29-229 at depth intervals 300–500 and 600–800 cm and core Va22-275 at a depth interval 500–600 cm: see Figure 1 for locations). Relative abundances (total counts) of different elements are plotted along the lengths of the two cores. The stratigraphic units are shown according to the original core logging (unpublished MESEDA data; cf. K. Steinkamp and D. Schumann, The chemical composition of sediments cores recovered during Valdivia Cruises VA01 and VA03 from the Atlantis II deep (Red Sea), unpublished data, 1974). (a) Variations are seen in the abundances of different elements at two different depths in core Va29-229 (300–400 and 700–800 cm). K correlates with Si in the upper part of the core (most likely in authigenic clays) but not in the lower strata where there may be more detrital input. Cu correlates with total sulfur in the sulfidic section, but not in the clay-rich section in SU1. Fe concentrations reflect the change from diffuse to sharp lamination with burial (i.e., the amplitude of varying Fe concentrations increase between adjacent laminae). (b) Core Va22-275 includes two sections with high Mn concentration and low Fe. In several sections, the core scans show alternating layers of Fe then Mn enrichment at the cm scale (see also Figure 4d). In other sections, Mn concentration correlates with Fe, most likely in authigenic carbonates. Ca, Si, and K correlate with Al in the section dominated by detrital sediment. Correlation between Zn and Fe most likely reflects adsorption of Zn onto Fe-(oxy)hydroxides. Open spaces in the core are indicated by low concentrations of all elements.

the sedimentary structures. The thin sections were examined in reflected and transmitted light and using a JEOL 6610LV scanning electron microscope (SEM). Spot analyses of discrete mineral phases were performed using the energy-dispersive spectrometer of the SEM and by element mapping using the JEOL 8230 SuperProbes at University of Ottawa and GEOMAR. Several samples were also studied using a Field Emission SEM (JSM-7500F FE-SEM) at the University of Ottawa and by synchrotron-XRF (VESPERS beamline) at the Canadian Light Source, following the methodology of *Feng* [2005] and *Feng et al*. [2007]. Details of these analyses are described further below.

The normative mineralogy was calculated for each sample based on bulk chemical data obtained at the University of Kiel. The full data set and the analytical methods are reported in *Laurila et al*. [2014a]. Sequential leaching experiments were also performed on selected samples to allow a more precise characterization

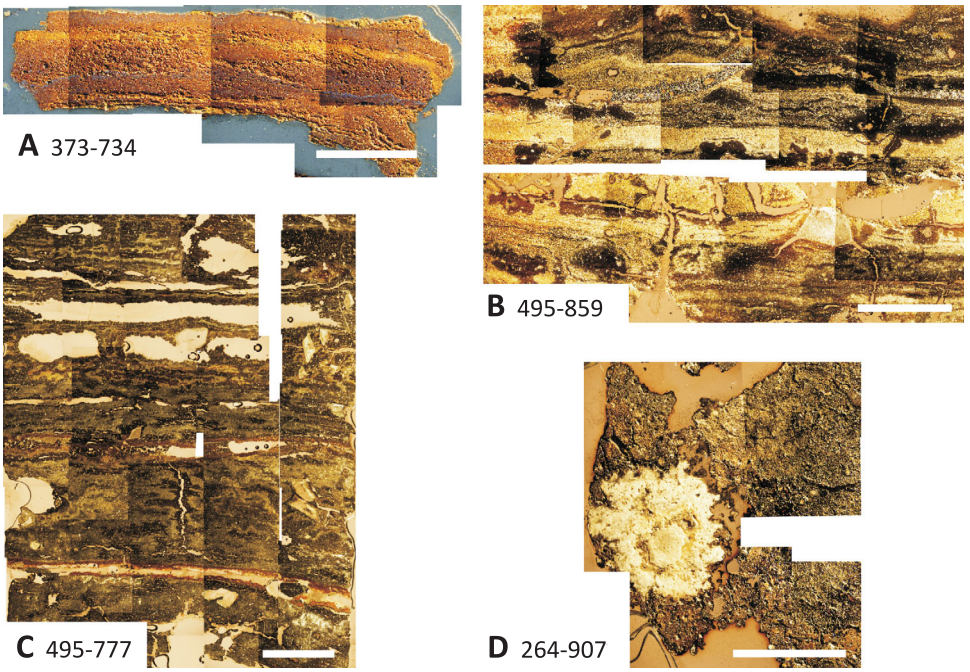

Figure 6. Photomicrograph mosaics of fine, millimeter-scale layering in the metalliferous sediment of the Atlantis II Deep, shown in normal and transmitted light (scale bar is 5 mm). (a) Sample from a laminated Fe-(oxy)hydroxide-rich layer in unit DOP (373-734). The different colors (from light yellow to bright orange and darker red) mainly reflect the proportion of Fe-(oxy)hydroxides and authigenic clays. (b) Laminated detrital-rich and sulfide-rich sediment from unit SU1 (495-859; Figure 4g). Lighter bands contain abundant fossiliferous detritus; darker bands are mixtures of detrital components and sulfidic components. Cracks that distort the primary layering are lined with darker minerals suggesting that they represent pore fluid conduits. (c) Sulfide-rich section (495-777) in unit SU1. Darker layers are sulfide rich; lighter layers contain abundant biogenic detrital silica but are also enriched in metals owing to their high permeability (see Figure 10). Alteration on microfractures may be evidence of fluid migration between permeable layers. White areas are void space. (d) Sulfide and metal-rich sample from unit SU1 (core 264 at 907 cm) showing an example of disseminated anhydrite (white) typical of cores in proximity to known venting.

of the nonsulfidic minerals, especially the different carbonates and Fe-(oxy)hydroxides and Mn-(oxy)hydroxides [e.g., *Tessier et al*., 1979; *Hall et al*., 1996; *Hlavay et al*., 2004; *Cappuyns et al*., 2007]. Four steps were performed in each experiment using (i) distilled water, (ii) ammonium acetate (0.1 *M* buffered to pH 4.7–4.9), (iii) cold hydroxylamine hydrochloride (0.1 *M* $NH_2OH{\cdot}HCl$ in 0.01 *M* HNO_3), and (iv) hot hydroxylamine hydrochloride (0.25 *M* $NH_2OH{\cdot}HCl$ in 0.025 *M* HNO_3 at 60°C). Each step removes a different suite of minerals that are soluble in the different leaches. The performance of each step was monitored by ICP analysis of the leachates at ALS Laboratories in Vancouver.

5. Results

The physical properties of the sediments observed in the core logs and XRF scans (e.g., color, grain size, and millimeter-scale layering: Figures 3–5) are closely linked to the hydrothermal input and diagenetic effects. Figure 5a (core 229) shows the variations in bulk composition in just 1 m of sediment in the upper units (SU2 to AM) and lower strata (SU1 to COS). The diffuse layering typical of AM is reflected in the lack of chemical variations, whereas in the lower strata, sharp changes in Fe, Si, and K are seen between the different laminae. The high Cu and Zn in SU1 correspond to the time when hydrothermal venting was located in the north of the Deep; they are much lower in SU2 and AM when hydrothermal venting shifted to the southwest relative to this core. Core 275, also in the northern part of the Deep, shows alternating layers of Fe then Mn enrichment at the cm scale (Figure 5b; see also Figure 4d). As many as five episodes of Mn-oxide deposition appear to have occurred over an interval of less than 20 cm, corresponding to previously unrecognized rapid changes in the chemistry of the brine pool.

Among the other sampled cores, well-defined laminations are common in the lower strata (e.g., Figures 4d–4g and lower section of Figure 5a). Millimeter-scale laminae of different colors (orange, yellow, and

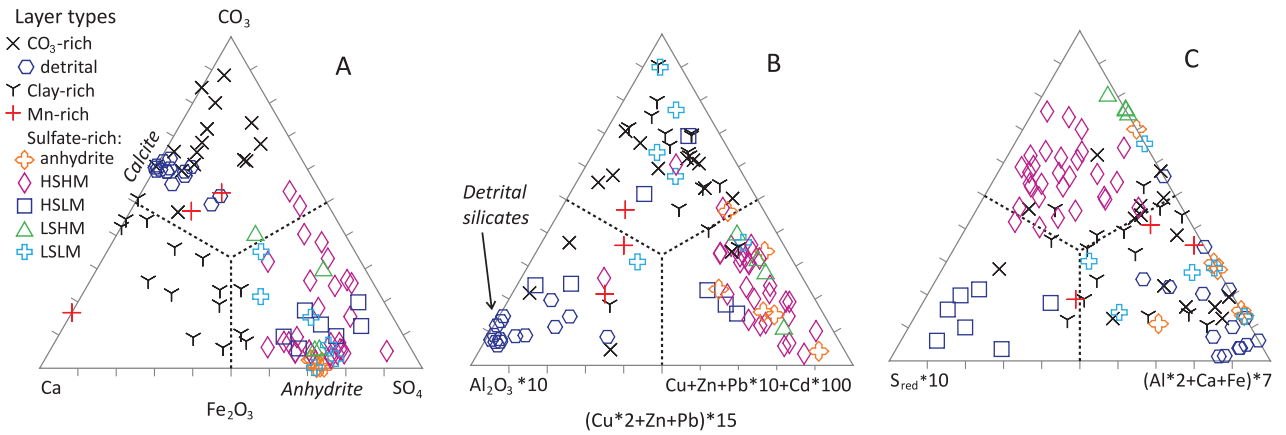

Figure 7. Classification of the Atlantis II Deep sediments according to major metal and nonmetal contents (data from *Laurila et al.* [2014a]). The samples considered in this study comprise three main types: carbonate-rich samples, clay-rich samples, and sulfate-rich samples. Carbonate-rich samples that contain mostly detrital biogenic carbonate plot close to calcite in (a). These samples contain abundant Al_2O_3 in aluminosilicates (b), which are also detrital. The clay-rich samples plot in the lower left of (a) because they contain neither abundant CO_3 nor SO_4; they are not particularly Ca rich, but the clay fraction may contain Ca. Many of the clay-rich samples and carbonate-rich samples are Fe rich (b), which reflects the abundance of Fe-(oxy)hydroxides but also Fe-rich clays (e.g., nontronite) and Fe-bearing carbonates; accordingly Fe-content cannot be used to discriminate between mineralogically different samples. The sulfate-rich samples contain both anhydrite and abundant secondary sulfates that were originally present in the cores as sulfides (see text for discussion). These samples contain the most base-metals and plot in the metal-rich corners of Figures 7b and 7c. Reduced sulfur (i.e., sulfur remaining in the samples as sulfides) was calculated from total sulfur minus sulfate sulfur (c); the calculated sulfide contents are minimum values, because of oxidation to sulfate. Samples with the most sulfide and sulfate can be further classified according to their metal-to-sulfur ratios (e.g., high sulfur, high metal [HSHM]; high sulfur, low metal [HSLM]; low sulfur, high metal [LSHM]; and low sulfur, low metal [LSLM]). The mineralogy of the HSHM samples is dominated by Zn-sulfides and Cu-sulfides and sulfate; HSLM samples include mainly Fe sulfides and sulfate. LSLM samples contain abundant Fe-(oxy)hydroxides and authigenic clays. LSHM samples have very low reduced sulfur but high nonferrous metal concentrations in a number of nonsulfidic metal-bearing minerals (see text for discussion). (Cu*2+Zn+Pb)*15 in Figure 7c and (Cu+Zn+Pb*10+Cd*100) in Figure 7b are different proxies for the nonferrous metal concentrations. (Al*2+Ca+Fe)*7 in Figure 7c is a proxy for detrital components, anhydrite, and Fe-oxyhydroxides. The compositions of the samples are plotted in moles; different scalars are applied for ease of visualization.

brownish red) can been seen in most Fe-(oxy)hydroxide layers (e.g., sample 373-734 from DOP, Figure 6a), whereas some metal-rich layers are green in color and contain abundant clays (Figure 4f). A small sulfidic component usually imparts a dark color to the laminations (as low as a few percent), and the sulfide-rich layers are typically black (sample 495-859 from SU1: Figures 4g and 6b). Microscopic grains of sphalerite and chalcopyrite occur in all of these layers, but the nonferrous metals are also highly concentrated in the finer-grained Fe-(oxy)hydroxide "matrix" of the sediment where discrete minerals cannot be seen. Other submillimeter, metal-enriched laminae contain abundant silica tests in a hydrothermal carbonate-rich and clay-rich matrix (e.g., dark grey layers in sample 495-777 from SU1: Figure 6c). Many sulfidic layers also contain anhydrite (e.g., sample 264-907 from SU1: Figure 6d).

The highest base metal contents (Cu+Zn+Pb+Cd) are found in layers with a high total sulfur content (both sulfides and sulfate, including abundant secondary sulfates; Figures 7a and 7b). Fe-rich layers are dominated by Fe-(oxy)hydroxides but also contain Fe-rich clays and Fe-bearing carbonates (Figure 7b). Different proportions of metals and sulfur are found: high-sulfur, high-metal samples (HSHM) contain abundant Zn-sulfides and Cu-sulfides and secondary sulfates (Figures 7a and 7b); high-sulfur, low-metal (HSLM) samples include mainly Fe sulfides; low-sulfur, low-metal (LSLM) samples contain mostly Fe-(oxy)hydroxides and authigenic clays; low-sulfur, high-metal (LSHM) samples have very low sulfide contents but still contain abundant metals as nonsulfidic metal-bearing phases (Figure 7c). The most metal-rich layers (both HSHM and LSHM) are found in SU1, SU2, AM, SOAN, and especially in SAM. Metal-poor but sulfur-rich (HSLM) layers, which contain mainly diagenetic pyrite, are dominant in the lower units, OAN and SU1. Anhydrite-rich layers are most common in SOAN and SU1. Biogenic calcite-rich layers are abundant in DOP, whereas hydrothermal carbonates are abundant in CO, and clay-rich layers are most common in CO, COS, and SU2.

5.1. Detrital Minerals

The background sediment contains about 20–45 vol % of detrital silicates. Quartz, feldspar, rock fragments, and mica were readily identifiable by SEM (e.g., Figures 8–10); more rarely heavy minerals were also observed (e.g., zircon, titanite in samples 264-474 and 373-734: see supporting information Table S3). The terrigenous clastic components are resistant to hydrothermal alteration and are well preserved in almost all layers. They are generally well crystallized and thus can be readily distinguished from the authigenic silicates.

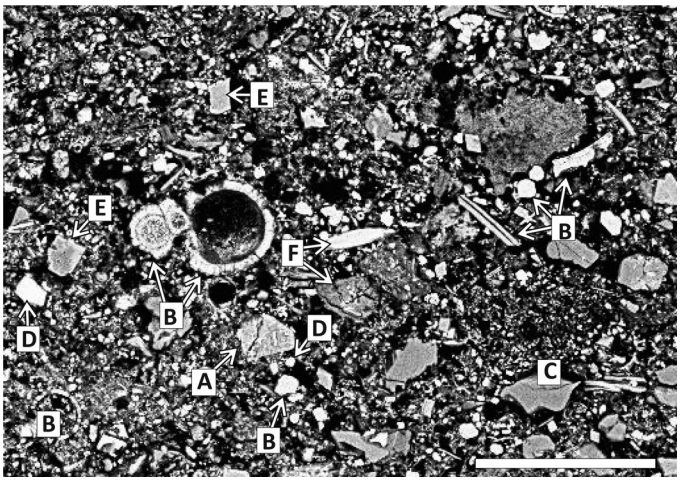

Figure 8. Backscattered electron image of a biogenic detrital layer from sample 495-859 (white layer in Figure 6b). The indicated detrital particles include (a) detrital aluminosilicate, (b) detrital biogenic calcite, and (c) detrital biogenic silica. Authigenic particles include (d) sulfide grains, (e) carbonates, and (f) metal-bearing clay-rich components. Scale bar is 100 μm.

Biogenic calcite comprises 30–65 vol % of the detrital input and can be distinguished from hydrothermal carbonate by the well-preserved fossil textures (e.g., Figure 8). Dolomite, which is more resistant to hydrothermal alteration than calcite, is also present in the detrital component but accounts for <10 vol % of the total carbonate. Locally, dolomite is found in the core zones of later hydrothermal Fe-Mn-rich carbonates, but clay-rich, sulfide-rich, or sulfate-rich layers contain only minor amounts of detrital carbonate.

Radiolarian tests are widely preserved in the detrital component, even in sediment with strong a hydrothermal overprint (e.g., SU1). They are often concentrated in discrete laminae (e.g., Figures 6c and 9a) that are highly porous and appear to have acted as thin aquifers for metal-enriched pore fluids, evident in the distinct Zn and S enrichment (Figure 10). Pseudomorphs of radiolarian tests show partial replacement and infilling by clay minerals (Figures 9a and 9b). The latter may have formed as a result of dissolution and reprecipitation of the biogenic silica. In Figure 9c, a radiolarian test has been replaced by an unidentified nonsulfide Zn-(oxy)hydroxide phase (e.g., sample 495-859 in supporting information Table S3).

5.2. Nonsulfide Authigenic Minerals

Fe-(oxy)hydroxides are found in all layer types, including sulfur-rich and metal-rich layers (Figure 9d), hydrothermally altered detrital layers (Figure 9e), and anhydrite layers (Figure 9f). The macroscopic color variations seen in core (bright red, yellow, and orange layers) mainly reflect the relative abundance of Fe-(oxy)hydroxides and clays. The poor crystallinity and extremely small grain sizes make positive identification generally difficult, but X-ray diffraction indicates a wide range of Fe-minerals among the better crystallized phases (e.g., samples 373-798 and 334-757: supporting information Table S4). The bright yellow layers commonly contain goethite (α-FeOOH), orange layers contain lepidocrocite (γ-FeOOH), and dark red layers sometimes contain hematite, which was positively identified by XRD in the lower sediments close to the known hydrothermal venting (sample 334-757, supporting information Table S4). Akaganeite (β-FeOOH), an Fe-(oxy)hydroxide mineral that can contain Cl in its structure, was also identified (sample 503-889: supporting information Table S4). Some samples that were bright orange at the time of sampling became brownish after drying (sample 421-870), typical of lepidocrocite [*Schwertmann and Cornell*, 2000]. Other layers, which were bright yellow turned dark red, consistent with abundant goethite (sample 421-223); others that were bright red at the time of sampling and remained so during sample preparation also consisted mainly of goethite (sample 503-626). Some of the color variations might be explained by grain size; smaller grain sizes, down to 0.2 μm, cause goethite to become notably darker [*Schwertmann and Cornell*, 2000], although the presence of minor hematite intermixed with goethite has the same effect.

In thin section, the Fe-(oxy)hydroxides commonly are observed as diffuse patches of Fe-enrichment in a poorly crystalline matrix (e.g., Figures 9b and 10). The diffuse nature of the Fe-enrichment is consistent with original deposition as amorphous material that later crystallized during diagenesis [*Taitel-Goldman and Singer*, 2002a,b]. The poorly crystalline phases contain subequal amounts of Si, Fe, and O with a few percent of minor elements (e.g., K, Cl, or S; samples 373-734, 495-859, and 264-474: supporting information Table S3). The more crystalline Fe-oxides (e.g., in Figure 9e) have bulk compositions closer to that of goethite or hematite (∼67% Fe and ∼33% O). Some have distinct rims that are enriched in Zn (>5 wt %) and Si (∼15 wt %) (sample 495-859: supporting information Table S3). This may indicate that the Fe-oxides could not accommodate Zn into their structure as they crystallized out of the original Si-Fe-OOH gel. Some of the

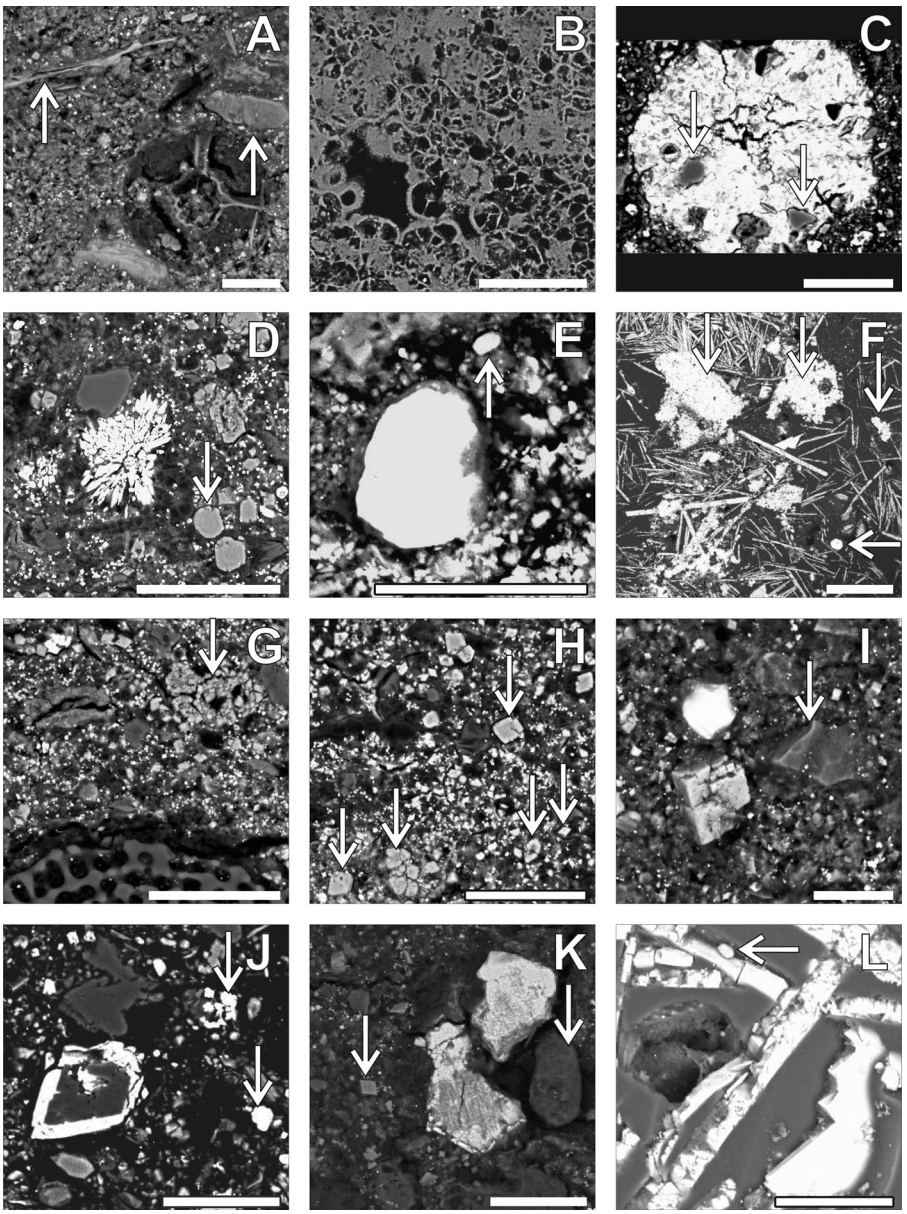

Figure 9. Backscattered electron images of detrital and authigenic components in different layer types of the Atlantis II sediments. All scale bars are 40 μm, except in F which is 400 μm. (a) Radiolaria fossil replaced by authigenic minerals (clays and carbonate) from a detrital and granular sulfide-rich section (264-907) in unit SU1. Arrows indicate detrital silicates (sheet-like biotite grain) and detrital quartz. (b) Densely packed radiolaria tests infilled with authigenic clays (dark areas) from a laminated Fe-rich section (373-734) in unit SU1. The silica framework of the fossils is replaced by Fe-(oxy)hydroxide minerals (light areas). (c) Large composite particle composed of Zn (up to ~45 wt %), oxygen (~25-45 wt %), S and Cl (up to ~7 wt % each), from 495-859 in unit SU1 (shown in Figure 6b). The arrows indicate authigenic clays. The rounded shape implies infill and replacement of a fossil remnant (radiolarian?). (d) Crystals of authigenic barite in a sulfide-rich section 495-777 in unit SU1 shown in Figure 6c. The arrow points to a Fe-(oxy)hydroxide particle. (e) Large Fe-oxide grain (goethite or hematite) with a thin rim of Si-Fe-(oxy)hydroxide containing ~6% of Zn and ~0.6% S. The arrow shows coexisting calcite, which would not have been preserved if the nonsulfidic phases were formed during core storage (sample 495-859). (f) Anhydrite crystals in an anhydrite bed from sample 503-254 in unit SOAN; downward arrows indicate Fe-(oxy)hydroxides, which are the most Zn-rich minerals in this sample (~1 wt % Zn). Horizontal arrow (lower right corner) indicates a barite crystal. (g) Zn-rich authigenic clay (arrow) containing ~5 wt % Zn and remnant of a radiolarian (bottom of photo) in a sulfide-rich section of sample 495-777 from unit SU1. (h) Authigenic Fe-Mn(-Ca)-carbonates (arrows) in the same sample (495-777). The carbonates are commonly zoned with Fe-rich rims and may contain few wt % Zn. (i) Euhedral (cubic) authigenic Fe-Mn(-Ca) carbonate in sulfide-rich section (264-907) in unit SU1. The brightest grain is pyrite; arrow indicates authigenic clay. (j) Zoned carbonate with dolomite core and rim of authigenic Fe-Mn(-Ca) carbonate from 495-859 in unit SU1. Arrows indicate pyrite grains. (k) Coarse-grained chalcopyrite with exsolution lamellae from a granular sulfide-rich section (264-907) in unit SU1. The arrows point to authigenic clay (dark grain) and carbonate. (l) Detail of anhydrite in Figure 9f. The arrow points to microscopic authigenic clay containing ~1 wt % Zn.

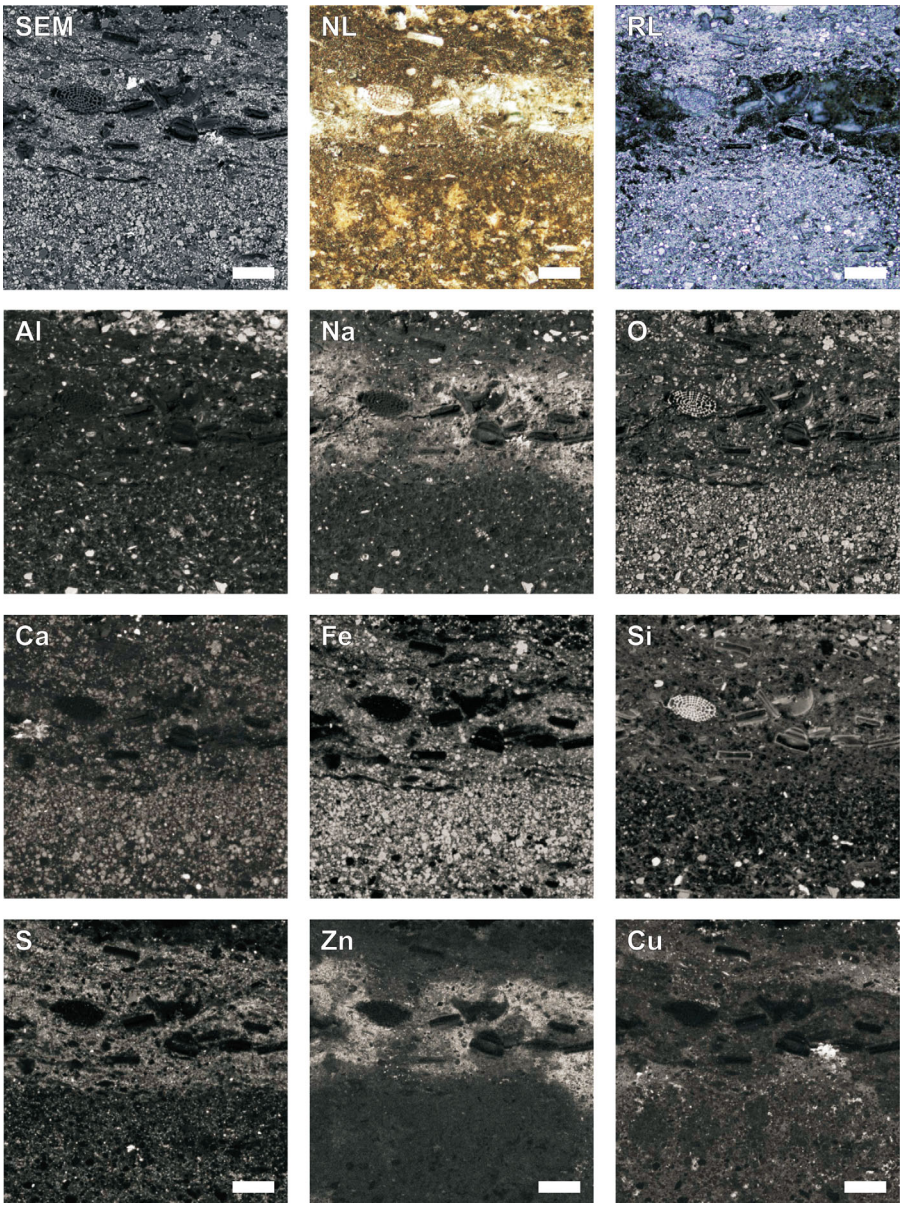

Figure 10. EPMA element maps of a sulfide-rich section of 495-777 from SU1 (shown in Figure 6c; SEM = backscattered electron SEM image; NL = normal light; RL = reflected light photomicrograph). The scale bar is 100 μm in all images. Aluminum is a proxy for detrital aluminosilicate minerals (including feldspar, mica, and rock fragments). The highest Ca concentrations correspond to calcite, but this layer (lower part of the image) also contains abundant Fe and O, most likely in authigenic carbonate. (top) The highest Si concentrations correlate with a permeable layer with abundant siliceous microfossils and clays. This layer also has high Zn and Cu concentrations, with moderate S (10–20 wt % S). Zn enrichment is confined to the middle of the S-rich band (a few tens of percent Zn), whereas Cu enrichment is found at the margins of the band. Na is also enriched in the permeable layer, consistent with the presence of salt from pore fluids.

amorphous phases are notably enriched in trace metals; for example, Figure 11a shows an EPMA element map of a cluster of rounded Si-Fe-OOH particles that are depleted in S but notably enriched in Ag, As, and Cd.

The Mn-rich layers are mainly fine grained and soft (Figures 4d and 5b) and composed mostly of amorphous Mn-(oxy)hydroxides. Black staining of adjacent layers is common, suggesting that some of the Mn has migrated out of the Mn-rich layers. Samples containing abundant Mn-(oxy)hydroxides generally do not contain abundant Fe-(oxy)hydroxides, confirming that conditions suitable for Mn precipitation alternated with conditions of Fe deposition. Crystalline manganite (MnOOH) was identified by XRD in samples from the most Mn-rich layers (e.g., sample 495-569 in CO: supporting information Table S4). Although Mn-carbonates

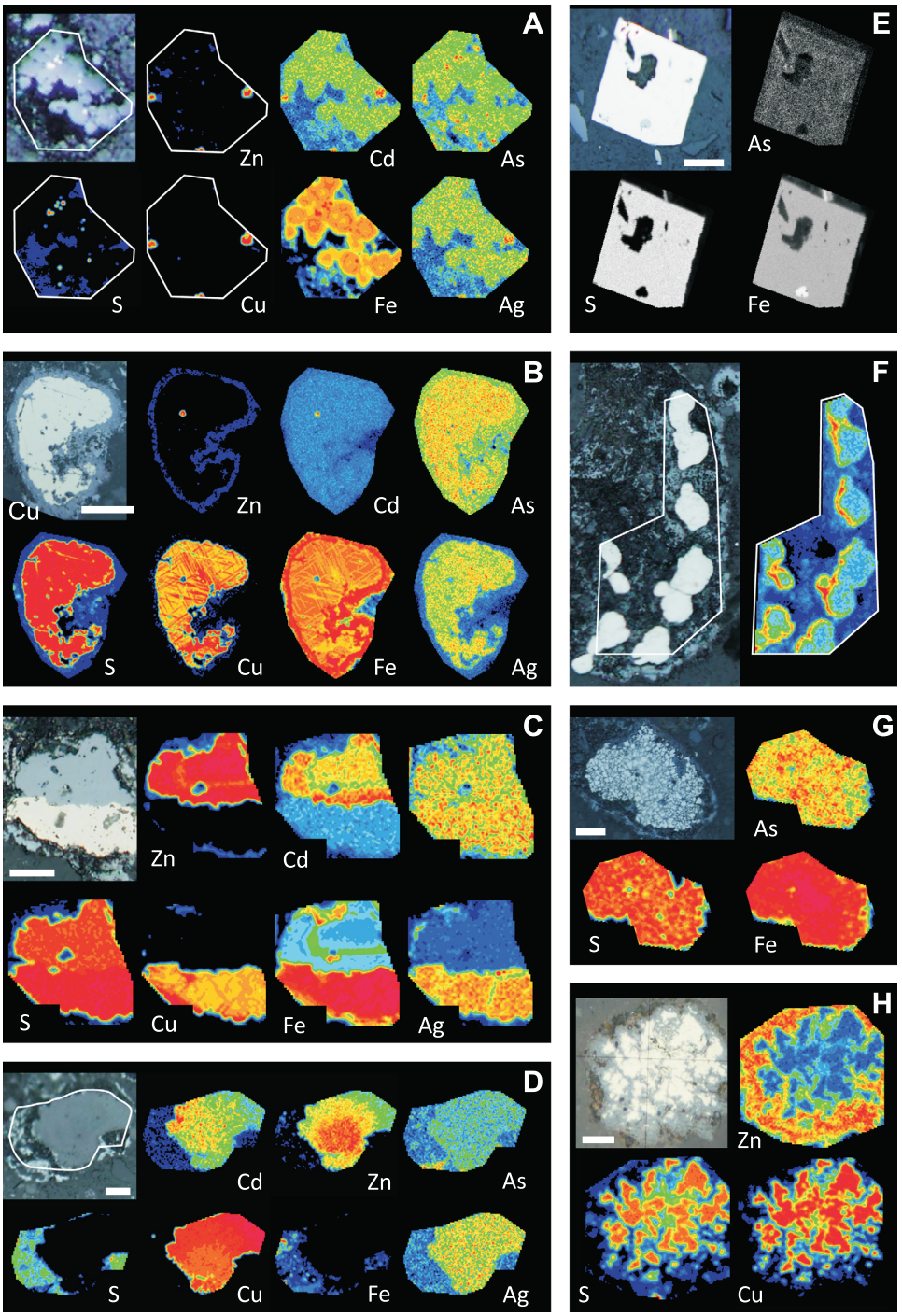

Figure 11. EPMA element maps of selected authigenic sulfide and nonsulfide particles in polished grain mounts. Scale bars are 20 μm, except in b and e, which are 50 μm. (a, f, and g) Sample 503-912 in the lower SU1 (with bulk concentration of 3.8 ppm Au and ∼17 wt % Zn+Cu) [*Laurila et al.*, 2014a]. (b–e and h) Sample 268-985 in unit CO (with 21 ppm Au and ∼17 wt % Zn+Cu: Oudin, 1987). (a) Cluster of Fe-rich authigenic clay particles. The clays contain more Ag, As, and Cd than the matrix. The highest As is found in pyrite inclusions (bright S-rich spots in the clays); the highest Ag and Cd are found in three Zn-rich and Cu-rich nonsulfidic particles. (b) Grain of chalcopyrite showing Cu-rich exsolution lamellae and a Fe-Zn-rich rim. A tiny inclusion of sphalerite is seen in the middle of the grain. (c) Composite grain of sphalerite and chalcopyrite. Cd is enriched in the sphalerite and Ag in the chalcopyrite. Sphalerite is zoned with varying Cd and Fe contents. (d) Nonsulfidic metal-enriched particle (most likely a metal-chloride) containing little or no Fe but high Cu, Zn, and Cd. The Cu concentrations are ∼45 wt % and the Zn content is <10 wt %. (e) Euhedral pyrite with low As content (<0.4 wt % based on counting statistics and comparison with microprobe data: supporting information Table S5). The relative concentrations of Fe, As, and S in this image are in grey scale. (f) Cluster of rounded (diagenetic?) pyrite grains with distinctive As-rich rims. The highest measured As content is 1.6 wt % As (supporting information Table S5). (g) Cluster of smaller As-rich pyrite grains from the lower strata. (h) Chalcopyrite that has been strongly altered during core storage.

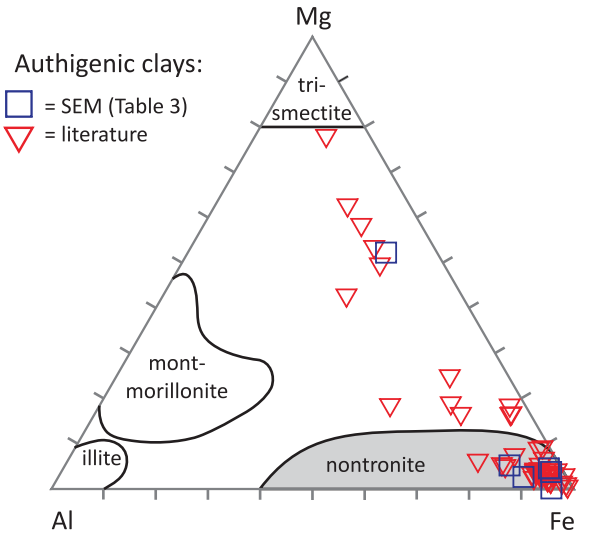

Figure 12. Compositions of clay minerals based on SEM spot analyses (supporting information Table S3), compared to data from previous studies (see supporting information Table S12). Nontronite is the most common authigenic clay, but Mg-rich clays are found in proximity to the known vents [*Zierenberg and Shanks*, 1983, 1988; *Singer and Stoffers*, 1987].

are present, most of the Mn-rich layers contain significantly more Mn than can be bound to the available carbonate.

Authigenic clay-rich layers are most common in the three uppermost units but are found in all stratigraphic units. Clay-rich layers in SU1 and SU2 have the highest metal contents (sample 264-474 in unit SU2: supporting information Table S3). They typically have a greenish color (Figure 4a, top, and 4f), are very fine grained, and are saturated with water with a high salt content. These layers had a distinctive "greasy" feel at the time of sampling, indicative of high primary pore water content (e.g., 508–512 cm in core 495 in Figure 3), and took several weeks to become completely dry (at 40°C). The clays are mainly amorphous or poorly crystalline, but they are readily distinguished from other silicates (e.g., detrital silicates in DOP) by their much lower Al/(Fe+Mg) (e.g., sample 264-474: supporting information Table S3 and Figure 12). The abundant pore water in the clay-rich layers likely accounts for the high K_2O content (~2.5 wt % in the most clay-rich samples), but some authigenic clays also contain K in their interlayers [e.g., *Bischoff*, 1972; *Butuzova*, 1984; *Badaut et al*., 1992]. All of the clay-rich horizons are enriched in Fe (Figure 7), partly because of codeposition with Fe-(oxy)hydroxides but also because of the presence of Fe-rich smectite (e.g., sample 264-474, supporting information Table S3). The latter is thought to have been typical of clays precipitated directly from the brine pool [*Zierenberg and Shanks*, 1983, 1988; *Cole*, 1988]. Spot analyses of the dark areas in Figure 9b, which is typical of the authigenic clays, indicate a bulk composition of ~45% O, ~20-30 wt % Fe, 10-15 wt % Si, and up to 15 wt % combined Mg, Al, and K (Figure 12, supporting information Table S3). In low-sulfide, high-metal (LSHM) samples, almost all clays contain at least a few weight percent metals and some up to 5 wt % Zn with no sulfur (e.g., sample 495-777, Figure 9g, supporting information Table S3).

Most of the silica in the sediment is present in the poorly crystalline Si-Fe-(oxy)hydroxides and authigenic clays. It is unclear how much silica was precipitated directly from solution and how much was released to the sediments from the poorly crystalline Si-Fe-(oxy)hydroxides during diagenesis. Increasing Si with depth in the cores (from less than 7 wt % Si in AM to >9 wt % in SU1 and DOP: supporting information Table S1) and high SiO_2/Fe_2O_3 ratios in sediment from in the lower strata (e.g., in samples 503-516 and 546-318) [*Laurila et al*., 2014a] suggest that silica was being deposited rather than dissolved during diagenesis.

Hydrothermal carbonates are common in CO and DOP, and in a few samples from SU1 and SU2. In some Mn-rich samples from DOP, most of the Mn is bound to carbonate (e.g., sample 495-889, which contains 9.3 wt % Mn and 11 wt % CO_2) [*Laurila et al*., 2014a]. In the darker carbonate-rich layers, biogenic calcite has been replaced by very small grains of dark or opaque Fe-Mn-carbonates (Figure 9h). As noted by others, the authigenic carbonates are readily distinguished from biogenic calcite by the Fe and Mn enrichment, the lack of fossil textures, and the more euhedral crystal forms (Figure 9i). They are commonly zoned but have widely varying compositions (Figure 13). Manganosiderite rims are common on earlier detrital carbonates (especially Mg-rich calcite or dolomite: Figure 9j), with the rims containing as much as ~40 wt % Fe and ~8 wt % Mn (supporting information Table S3). Many of the Fe-rich and Mn-rich hydrothermal carbonates also contain a few weight percent of Zn (sample 495-777 in Figure 9h, supporting information Table S3), consistent with a hydrothermal origin.

A variety of efflorescent salts of the form $MeSO_4 \cdot nH_2O$ are also present in the cores, in particular Zn-sulfates. These are interpreted to be mainly secondary minerals formed during core storage, either by oxidation of preexisting sulfides or by direct precipitation from metal-enriched pore fluids (e.g., see

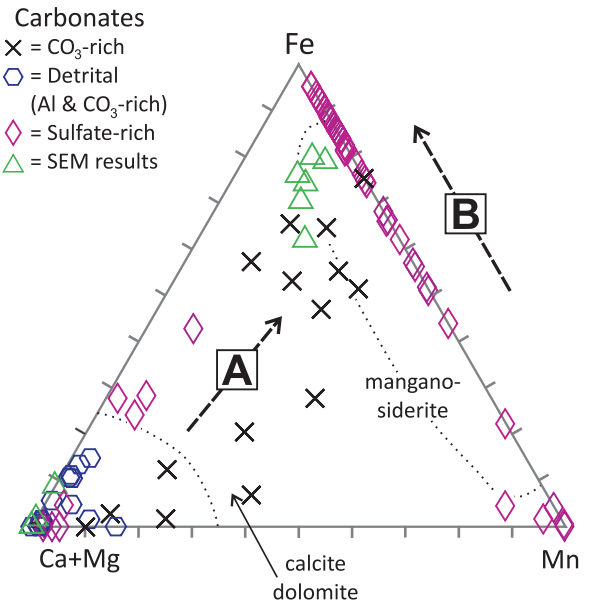

Figure 13. Compositions of carbonate minerals based on normative mineralogy (see text for discussion and supporting information Table S6). Detrital carbonate-rich samples plot close to the Ca+Mg corner, consistent with the abundance of calcite and dolomite in these samples. Other carbonate-rich samples, with a low detrital component, span the compositional field from Ca-Mg rich to Mn and Fe rich, consistent with the compositions of hydrothermal carbonate. Trend A represents increasing hydrothermal influence and decreasing total carbonate. Trend B represents changes in the hydrothermal carbonate from vent distal to proximal. Normative carbonate in all other hydrothermal samples (sulfate-rich) plots along the Fe-Mn line, closer to Fe than Mn, consistent with the presence of Fe-rich authigenic carbonate (supporting information Table S3). No other compositional data for the Atlantis II carbonates are available in the literature.

supporting information Data). Some authors have described minerals such as chrysocolla, atacamite, and hydrozincite [*Bischoff*, 1969; *Butuzova*, 1984; *Oudin et al*., 1984; *Gurvich*, 2006], which we interpret here to be secondary.

5.3. Sulfides and Sulfate Minerals

The sulfide-rich layers in the vent-proximal cores have been the focus of previous studies of the ore mineralogy because of the large grain sizes amenable to heavy mineral separation [*Stephens and Wittkopp*, 1969; *Pottorf and Barnes*, 1983; *Oudin et al*., 1984; *Missack et al*., 1989]. However, in most of the samples from this study, few sulfide grains were detectable without a microscope. Commonly, no sulfide grains can be seen in the diffuse patches of metal enrichment in the "matrix" of the sediments (Figure 10). Where visible, composite grains of sphalerite and chalcopyrite are common (Figures 11c and 14a), although many are altered (e.g., Figures 14b and 14c). The sphalerite grains show strong Fe/Zn zonation and high Cd concentrations (Figure 11c, upper part), although our data show lower Fe contents compared to some earlier studies (Figure 15 and supporting information Table S5). If all of the Cd in the sediments is contained in sphalerite, the concentration of Cd in the sphalerite would be ~0.2 wt % (Figure 16a); the Hg content would be ~30 ppm (Figure 16b). Some large chalcopyrite grains have exsolution lamellae with variable Fe/Cu ratios (Figures 9k and 11b), similar to the intermediate solid solution (ISS) previously documented by *Pottorf and Barnes* [1983] and *Missack et al*. [1989]. In a number of samples, chalcopyrite is also notably enriched in Ag (Figures 11b and 11c), with an estimated Ag concentration of ~0.3 wt % (Figure 16c). Galena was not found in the samples from this study.

Most of the pyrite in the sediments is spongy or framboidal, consisting of clusters of tiny, <1 μm grains (e.g., Figures 14d and 14e). Coarse subhedral to euhedral pyrite (up to 200 μm, Figure 11e) is mainly found in sediment closest to the inferred vent sources in SU1 and SU2. *Brockamp et al*. [1978] showed that the framboidal pyrite in the sediments likely grew around a nucleus of other Fe-rich particles (in some cases Fe-monosulfide), with the sizes of the clusters generally increasing with depth in the cores (e.g., Figures 14e and 14f). The framboidal pyrite typically has much higher trace metal concentrations than the coarse euhedral pyrite (e.g., Figures 11e and 11g), commonly with distinctive As-rich rims (Figure 11f). The As contents in the rims (up to 1.6 wt % in sample 503-912: supporting information Table S5) are about 4 times higher than in the cores, suggesting diagenetic enrichment during the growth of the pyrite. Sample 503-912 also has a very high gold content (3.8 ppm Au in the bulk sample) [*Laurila et al*., 2014a], consistent with coenrichment of As and Au in the rims.

Several gold-rich samples were studied under the FE-SEM, a surface technique, and with powerful X-rays by synchrotron-XRF. No evidence of Au nanoparticles was observed on the surfaces of pyrite or other sulfide grains under FE-SEM. Figure 17 shows the synchrotron-XRF maps of two samples, one containing a grain of As-rich pyrite (sample 503-912) and another containing chalcopyrite, secondary Cu and Zn phases, and authigenic clay (sample 268-985). The SXRF mapping was performed on the VESPERS beamline at the Canadian Light Source. High-energy X-rays were modified to have a photon flux of 5–30 keV. The XRF

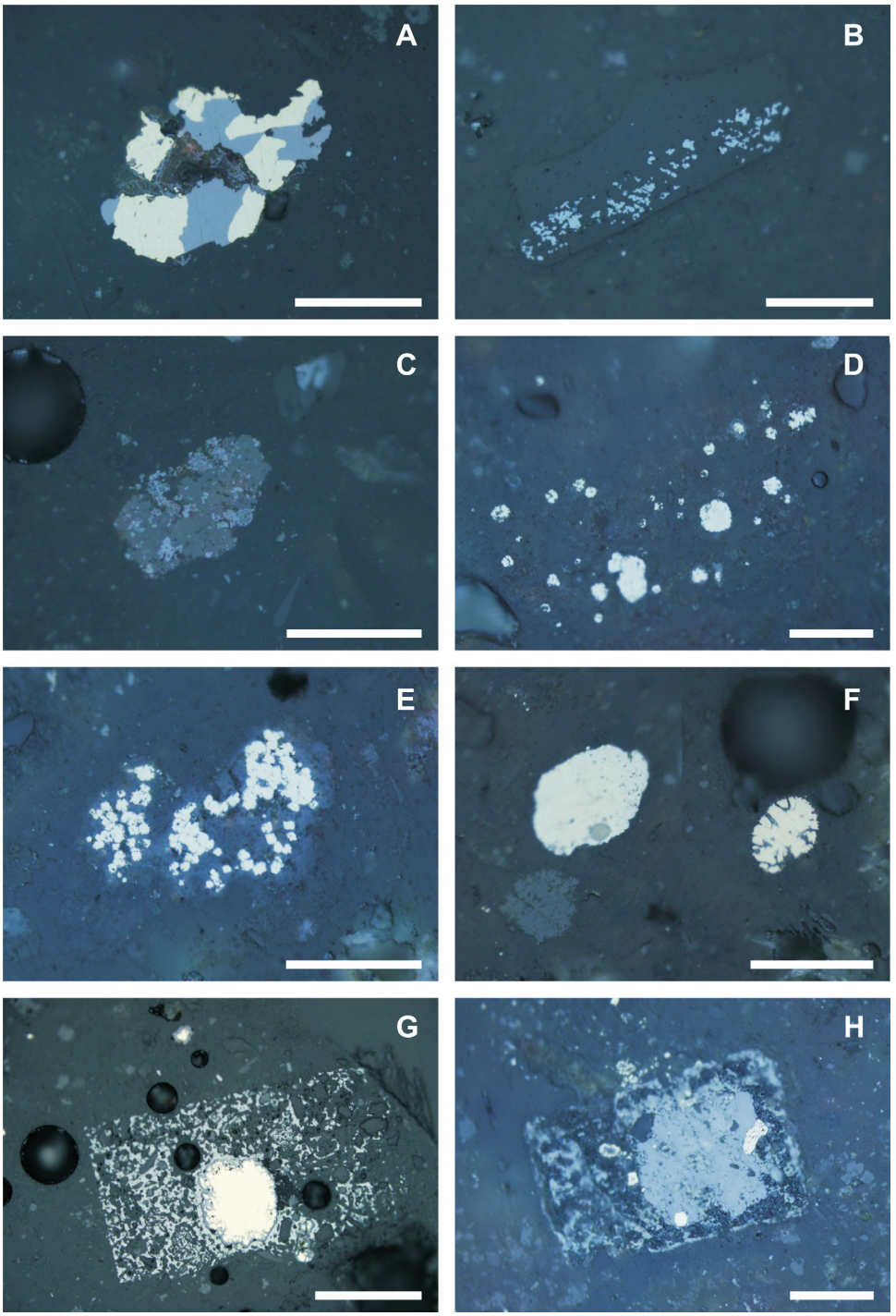

Figure 14. Reflected light photomicrographs of selected sulfide minerals (a–c, g) from sample 268-985 in unit CO and (d–f, H) from sample 503-912 in SU1. Scale bars are 50 μm, except in g, which is 200 μm. (a) Typical composite sphalerite-chalcopyrite grain. (b, c) Partly dissolved sphalerite grains caused by oxidation during core storage. In Figure 14b, the original shape of the grain is hardly visible, whereas in Figure 14c, sphalerite has been partly replaced by secondary phases. (d–f) Show different forms of diagenetic pyrite. (d, e) Clusters of framboidal pyrite grains of different size. (f) Single rounded grains of pyrite (nodular?) composed of tight clusters of smaller pyrite grains. (g) Rounded grain of chalcopyrite rimmed by Fe-rich and Zn-rich nonsulfide alteration. (h) Nonsulfidic, Pb-rich particle (grey) and, small pyrite grains (white) with As-rich rims (not shown). The rectangular shape of the alteration halo in Figures 14g and 14h is a common feature and may reflect secondary metal-sulfates that have pseudomorphed dissolved anhydrite or salt.

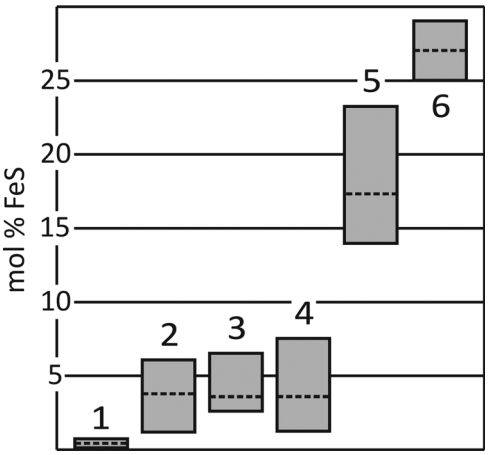

Figure 15. Range of Fe contents in sphalerite from metalliferous sediments of the Atlantis II Deep. Lower and upper limits of the boxes are minimum and maximum values; the dotted lines indicates averages. (1) Low-Fe sphalerite from a distal core 495 in unit SU1 (supporting information Table S5). (2–5) Fe-rich sphalerite from SOAN, CO, and OAN [from *Pottorf and Barnes*, 1983]. (6) Rare marmatite from the sulfide facies studied by *Stephens and Wittkopp* [1969]. All samples are from cores in the Southwest Basin.

spectra were recorded with a SII NanoTechnology Vortex single-element Si-drift detector (SDD) positioned at 45° to the sample, 90° to the incident beam, and 15.2 mm from the sample. We used a ~2 μm diameter beam with a dwell time of 2 s and step sizes of 3 μm. The high-energy X-rays of the synchrotron penetrate ~100 μm into the sample, and even a few Au nanoparticles in this volume would be detected by this method [e.g., *Basto et al*., 1995; *Brugger et al*., 2010]. In most of the samples, the Zn, As, Fe, and Au maps of the pyrite completely overlap, precluding the detection of Au. However, the authigenic clay in 268-985 shows the distinct Lγ1 peak of Au in the absence of the doubling peak of Fe at the same energy. This is a good indication of possible nonsulfide Au enrichment in the clay.

The anhydrite layers examined in this study consist of almost pure anhydrite. Although the layers may be up to several meters in thickness, most are less than a few tens of centimeters thick. Some anhydrite layers are well consolidated and fine grained (Figures 4c and 4h); in others, clusters of anhydrite have coprecipitated with hydrothermal clays and Fe-(oxy)hydroxides and locally with minor barite or sulfides (Figures 9f and 9l). Multiple thin layers (<2 cm) are commonly found, rather than single coherent beds, and they have diffuse contacts with adjacent layers. Barite (<2 vol %) is found in cores close to the hydrothermal vents. It has a distinctly crystalline habit (Figure 9d) and appears to have grown within the sediments.

5.4. Quantitative Mineralogy

After correcting for salt content, we calculated the normative abundance of the minerals in each layer type from their bulk chemical compositions (see supporting information Table S6). The siliciclastic detrital component was estimated by assuming that ratios of immobile elements (e.g., Al, Zr, Ti, and Sc) are constant and similar to those of average shale (PAAS from *Taylor and McLennan* [1985]). Good correlations between Sc and the concentrations of Al, Si, and K in the samples ($r^2 = 0.97$, 0.80, and 0.50, respectively) allowed us to estimate the amount of these elements in the siliciclastic detrital component using the Sc/element ratio of PAAS. Sediment layers with the largest detrital input contain about 35 wt % siliciclastic material; all other layer types contain less than 10 wt % (<5 wt % in the clay-rich and anhydrite-rich layers). Nondetrital silica (in excess of PAAS) accounts for about 10–15 wt % of all sample types, except in the Mn-oxide and anhydrite layers that typically contain <2 wt % nondetrital SiO_2.

In samples with molar $CO_3 > SO_4$, calcite was first estimated from the Ca content, and the balance of the Ca was attributed to anhydrite; in samples with molar $SO_4 > CO_3$, the anhydrite content was estimated first and the balance of the Ca attributed to calcite. Any residual Ca was assumed to be present in clays. In many carbonate-rich samples, molar Ca is less than or equal to the molar CO_3. In these samples, the residual CO_3 correlates well with nondetrital Mg ($r^2 = 0.57$), consistent with the presence of dolomite (reported in supporting information Table S6 as end-member $MgCO_3$). Any residual CO_3 after calcite and dolomite formation was attributed to $MnCO_3$ (according to the bulk Mn content) and the remainder to $FeCO_3$. The results show that layers rich in detrital carbonate contain as much as 65 wt % of carbonate minerals (~90% biogenic calcite and ~10% Mg-carbonate). The most carbonate rich of the hydrothermal layers contain about 20 wt % Fe-carbonate and Mn-carbonate, with only minor Ca-carbonate. Other metal-rich layers typically contain ~10 wt % authigenic carbonate, and clay-rich layers contain <5 wt % carbonate (both detrital and authigenic). Any Mn left over from the Mn-carbonate calculation was assumed to be present as Mn-oxides (<2 wt % MnO for all samples except in the most Mn-rich layers).

The samples with molar $SO_4 > CO_3$ contain up to 15 wt % anhydrite (although some $CaSO_4$ may be secondary gypsum: see below). Barite was assumed to account for all the Ba in the samples, but is never more than

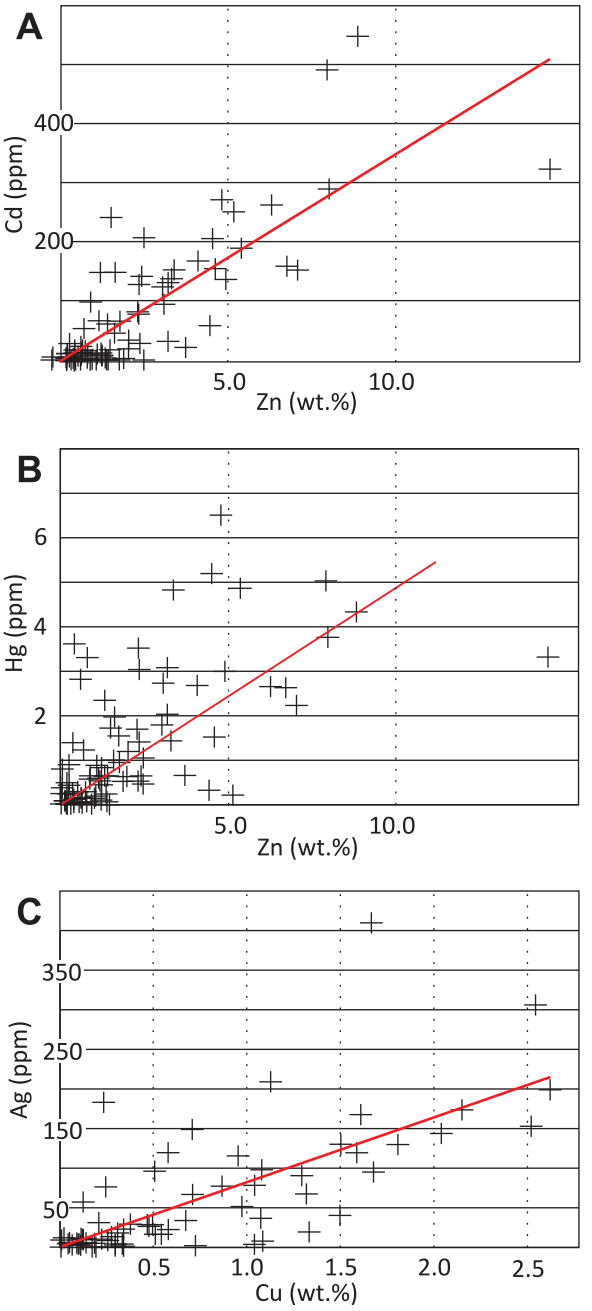

Figure 16. Biplots of Cd versus Zn, Hg versus Zn, and Ag versus Cu in bulk sediment samples from the Atlantis II Deep (data from *Laurila et al.* [2014a]). (a, b) Trend lines show possible Cd (~0.2 wt %) and Hg (~30 ppm) concentrations in sphalerite, assuming all metal is contained in sphalerite. (c) Trend line of possible Ag concentration in chalcopyrite (~0.3 wt %) if all Ag is in chalcopyrite (e.g., suggested by Figures 11b and 11c).

a few weight percent. Many samples have a higher molar amount of SO_4 than Ca and Ba combined, confirming the presence of secondary metal-sulfates. In these samples, the reduced sulfur content (calculated from total sulfur and sulfate) [*Laurila et al.*, 2014a] is a minimum value. Reduced sulfur was first attributed to $CuFeS_2$, based on the Cu content of the samples, then FeS_2, and finally ZnS. For the purposes of the normative calculation, we assumed that all Zn that is now present as secondary Zn-sulfates was originally present in the samples as sphalerite, so any residual sulfur after the formation of anhydrite was attributed to oxidized ZnS. This is supported by the strong coenrichment of Zn in sulfate-rich samples with trace metals normally associated with sphalerite (e.g., Cd). In many samples, the total amount of sulfur in sulfide and secondary sulfates was far less than that needed to bind the Zn and Cu as sulfides (supporting information Table S6). Any sulfur remaining after the formation of these minerals was attributed to additional pyrite, and all Fe remaining after the formation of pyrite, chalcopyrite, and siderite was assumed to be present in Fe-(oxy)-hydroxides and Fe-rich authigenic clays (reported as Fe_2O_3 in supporting information Table S6).

The calculated mineral abundances indicate that the clay-rich layers are dominated by Fe-(oxy)hydroxides and aluminosilicates but also contain about 5 wt % anhydrite, 1 wt % pyrite, and 1 wt % of other sulfides. The hydrothermal carbonate layers contain about 10 wt % sulfides, mostly pyrite, and the most metal-rich layers contain about 15 wt % sulfides, with subequal amounts of sphalerite, chalcopyrite, and pyrite. Detrital layers contain about 2 wt % pyrite and 0.5 wt % of other sulfides. A nontrivial component of residual Zn and Cu (up to 5 wt % Zn and 1 wt % Cu) was found in many of the most metal-rich samples with insufficient reduced sulfur or sulfate to account for all of the Zn as ZnS or Cu as $CuFeS_2$ (supporting information Table S6). Figure 18 summarizes the results of the calculations, showing the relative proportions of the major components of different layer types plus the weight percent of sulfide and nonsulfide metal-bearing minerals.

5.5. Sequential Leaching Experiments

Sequential leaching experiments were performed on 33 representative samples to better characterize the Fe-(oxy)hydroxides, carbonates, and other nonsulfide minerals. The first leaching step used distilled water,

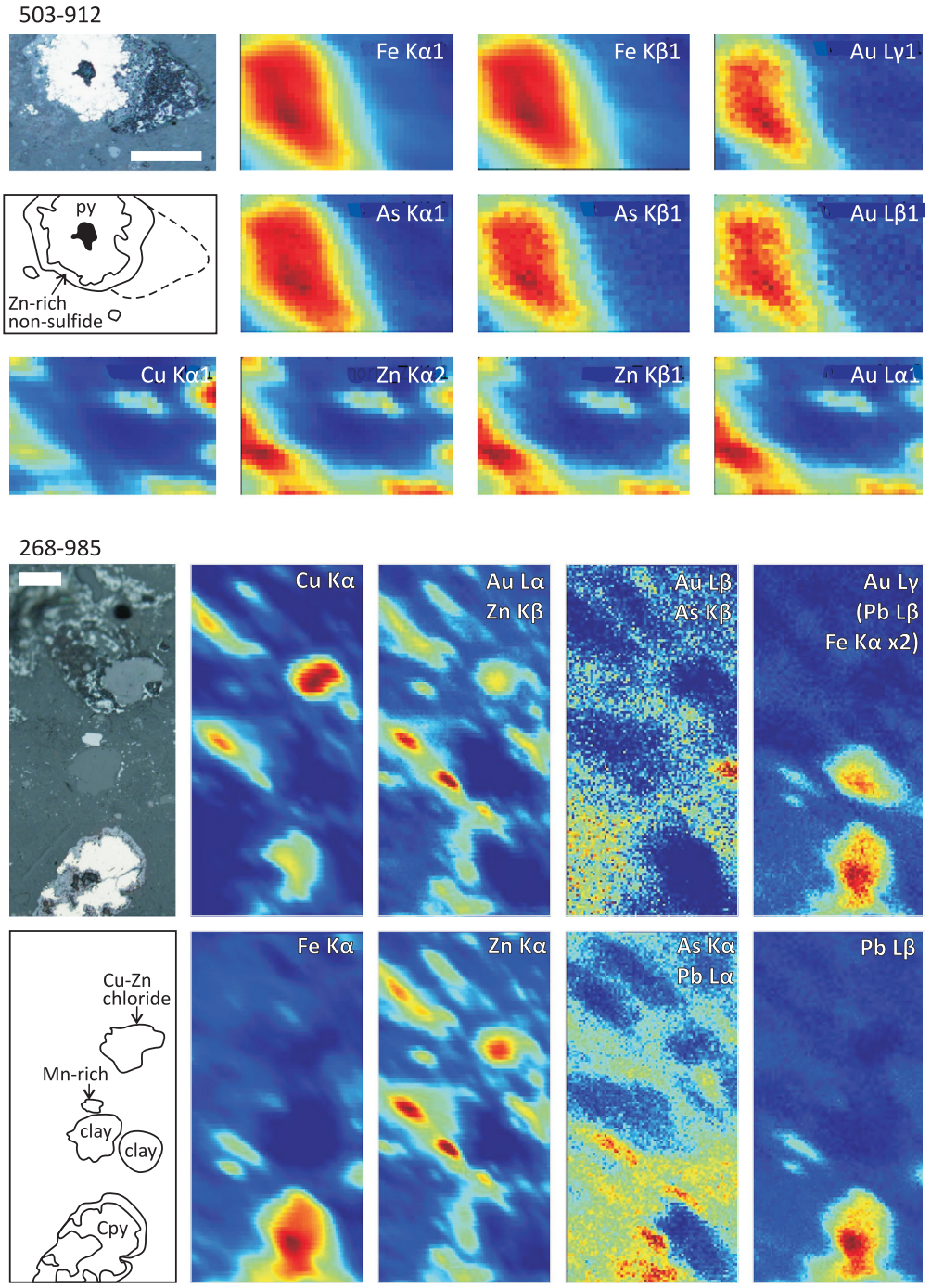

Figure 17. Synchrotron-XRF element maps of coexisting As-rich pyrite and nonsulfide particles in polished grain mounts. Analyses were performed on the VESPERS beamline at the Canadian Light Source [*Feng*, 2005; *Feng et al*., 2007]. The VESPERS beamline delivers a focused hard X-ray beam to solid materials so that a microscopic volume can be analyzed by X-ray fluorescence (XRF). The sample is mounted at a 45° angle to the Si-drift detector resulting in oblique images of the sampled volume, which are presented here as 2-D XRF maps. (top) (sample 503-912) Shows a pyrite grain rimmed by a secondary nonsulfide Zn phase (up to 15 wt % Zn). (bottom) (sample 268-985) Shows a chalcopyrite grain surrounded by a similar nonsulfide Zn phase, a separate Cu-Zn-rich phase (up to 45 wt % Cu, possible chloride?), two authigenic clay minerals, and a small Mn mineral. The scale bars are 50 μm in both images. In 503-912, Zn and Cu in the S-XRF maps correlate with the surface expressions of the target grains, but Fe and As concentrations reflect the penetration of X-rays below the sample surface. In this sample, the Kβ1 peaks of As at 11726 eV and Zn at 9572 eV overlap with the Lα1 and Lβ peaks of Au at 9713 and 11441 eV, and the doubling peaks of Fe at 12807 and 14115 eV raise the background around the Lγ1 peak of Au at 13381 eV, precluding the detection of Au. However, in 268-985, one of the authigenic clay minerals shows the distinct Lγ1 peak of Au that is not matched by the Kα doubling peak of Fe at the same energy (Fe Kα x2). The lack of correlation with Fe and As in this grain is a good indication of possible nonsulfide Au enrichment.

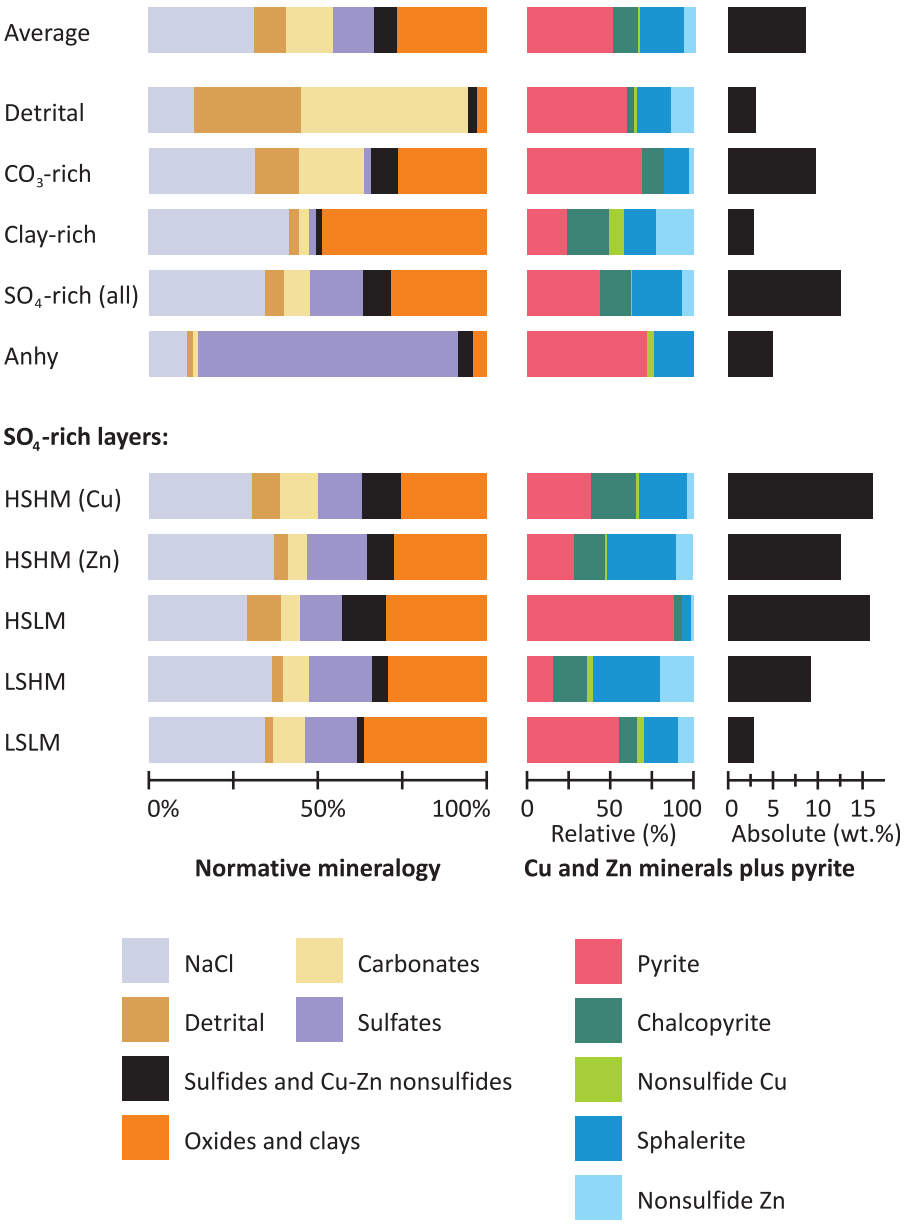

Figure 18. Summary of the normative mineralogy of the Atlantis II metalliferous sediments (data from supporting information Table S6). (left) The proportions of major minerals in different layer types. NaCl refers to salt crystallized from pore water in the samples during drying. (middle) The relative abundances of sulfide and nonsulfide Cu and Zn minerals, plus pyrite, in the different layer types (corresponding to the black bar on the left). (right) The total amounts of sulfide and nonsulfide Cu and Zn minerals (in wt %).

which dissolves anhydrite, secondary salts, and other water-soluble sulfates. The second step used ammonium acetate, which mainly dissolves calcite and dolomite, some Cu-carbonates and Zn-carbonates, but not the Fe-carbonates or Mn-carbonates. The third step used cold hydroxylamine hydrochloride, which dissolves Mn-(oxy)hydroxides and Fe-(oxy)hydroxides and Fe-Mn-carbonates, but the most insoluble carbonates (e.g., siderite) remained in the residue. The fourth step treated the samples with hot (60°C) hydroxylamine hydrochloride, which dissolves the more resistant Mn-(oxy)hydroxides and Fe-(oxy)hydroxides; ferrihydrite, goethite, and lepidocrocite are leached but not crystalline Fe-oxide minerals such as hematite and magnetite. The leachate data for each step (normalized to 100%) are reported for representative samples of different layer types in supporting information Tables S7, S8, and S9. The cumulative proportions of different elements dissolved by all four steps are listed in supporting information Table S10, and the complete data set for all 33 samples is provided in supporting information Table S11.

The dissolved elements in the first leaching step for all samples correlate well with Na in the bulk samples [*Laurila et al*., 2014a], confirming that most of the leachable components (e.g., Ca, Mg, and K) were contained in salt. The ratios of the major cations (Ca:K:Mg:Mn) in the leachates were also similar to those of the Lower Brine and pore water [*Anschutz et al*., 2000; *Pierret et al*., 2001]. Most of the anhydrite was removed by the first leaching step, except in the most anhydrite-rich samples (supporting information Table S9). In these, the total dissolution of anhydrite was not achieved until the second leach, suggesting that the distilled water became saturated with $CaSO_4$ quite quickly or that the kinetics of anhydrite dissolution were sluggish. The concentration of Mn in the first leachate varied greatly between sample types, but some Mn compound(s) were clearly soluble in water. In some samples, the pH of the first leachate decreased rapidly, most likely due to dissolution of acid-producing compounds such as metal-sulfates, whereas in the carbonate-buffered and/or metal-poor samples, the pH of the solution remained near neutral (supporting information Table S11).

The majority of the elements leached from the carbonate-rich samples were removed in steps 2 and 3. In the detrital carbonate samples, up to ~90% of the Ca was removed (supporting information Table S7). In some of these samples, a large proportion of the Cu and Zn were also apparently bound to carbonate. Samples with high CO_3 contents but lacking calcite (e.g., samples 546-180 and 503-889: supporting information Table S7) were less affected by the second leaching step. In these samples, Fe (and Mn) were only leached during steps 3 and 4 (e.g., in sample 503-889 most of the Fe was not leached, and 36% of the Mn remained undissolved). For some Mn-rich samples (e.g., 495-569), the total of Mn leached during steps 2–4 was much larger than the molar amount of CO_3, consistent with the presence of soluble Mn-oxides. Although significant amounts of Fe were leached from the Fe-(oxy)hydroxide and Mn-(oxy)hydroxide samples, very little of the Fe-(oxy)hydroxides identified as goethite by XRD were leached by either cold or hot hydroxylamine hydrochloride (e.g., only 1% of the Fe was found in any of the leachates from sample 495-569, which contains abundant goethite according to XRD). This may be explained by the presence of extremely fine-grained and insoluble "nanohematite," which is difficult to distinguish from goethite by XRD (e.g., as previously noted by *Schwertmann et al*. [1998]). Samples in which akageneite and lepidocrocite were identified by XRD had the largest leachable fraction of Fe (e.g., samples 421-870 and 503-889).

Sulfides were resistant to dissolution in all steps of the experiments, but 75–100% of the Zn (and less Cu) was found in the leachates of most sample types (supporting information Table S10). A strong correlation between total dissolved metals, especially Zn, and nonanhydrite SO_4 in the first leaching step ($r^2 = 0.61$) is consistent with the presence of abundant secondary $ZnSO_4$ in the samples. Trace metals normally associated with sphalerite (e.g., Cd) were also dissolved with the $ZnSO_4$. The amount of metal dissolved by distilled water also correlated well with the measured pH of the first leachate ($r^2 = 0.80$ for Cu and 0.63 for Zn in all 33 samples), reflecting the presence of acid-producing efflorescent salts. Although many of the samples contained pore water brine that could have contributed to the water-soluble Zn, the maximum contribution would have been less than 1 wt % [cf. *Anschutz et al*., 2000].

Almost all of the Zn was leached from the high-sulfur, high-metal samples (HSHM samples) in the first step, but only about half was leached from the low-sulfur, high-metal samples (LSHM samples) (supporting information Table S9). This is consistent with the presence of Zn-rich insoluble nonsulfide minerals in the low-sulfur samples. In the high-sulfur, low-metal (HSLM) samples, about half of the Ni and Co was leached by the final step, but less than 10% of the As, Mo, Sb, Ga, and Sn, consistent with these elements residing in insoluble pyrite. Pb in the HSLM samples was also retained in the residue, although the total concentrations are low. In the Cu-rich samples, Ag was not leached, consistent with Ag being mostly in insoluble chalcopyrite. In 90% of the samples, Au was completely insoluble (supporting information Table S10), confirming that it is mostly present in insoluble sulfides or clays. However, Au was detected in four samples after the first leach, suggesting that in these few cases Au was present in secondary salts or weakly adsorbed onto clays. Seventy-three percent of the gold was leached from one clay-rich sample (373-8 with a total salt-free gold content of 575 ppb Au) and 39% of the gold from another (495-362 with total salt-free gold content of 1041 ppb Au) [*Laurila et al*., 2014a]. These samples did not contain significant leachable Zn or Cu, suggesting that the Au was probably not present in secondary metal-sulfates.

6. Discussion

6.1. Formation of Fe and Mn Minerals

The dominant Fe precipitation in the brine pool occurred via oxidation of reduced iron to Fe-OOH at the chemocline between the Lower and Upper Brines. *Taitel-Goldman and Singer* [2001] suggested that the different Fe-minerals (e.g., goethite, ferrihydrite, and hematite) reflect formation in different parts of the brine pool, whereas *Butuzova et al*. [1990] and *Blanc et al*. [1998] concluded that the differences were mainly due to diagenetic transformation of ferrihydrite to goethite (or hematite in closest proximity to the vents) [see also *Schwertmann and Murad*, 1983]. The noncrystalline Si-Fe-OOH phases that are accumulating in the AM unit today are thought to be flocculated and then stabilized by Si-Fe-O bonds, which would have retard the formation of goethite [*Cornell et al*., 1987; *Schwertmann et al*., 1998; *Taitel-Goldman and Singer*, 2001]. *Taitel-Goldman and Singer* [2002a,b] reproduced these particles in the laboratory and found that the high Si in the Lower Brine (26 ppm) [*Anschutz and Blanc*, 1995b] likely contributed to their stability. However, the detailed composition and structure of the particles remain poorly known. Although goethite or ferrihydrite have been considered the dominant minerals formed from the gels, the sequential leaching experiments did not dissolve Fe in steps that would have removed these phases, suggesting a more stable phase (e.g., nanohematite) is now present in the cores. This is consistent with the Mossbauer data of *Schwertmann et al*. [1998].

Currently Mn-(oxy)hydroxides dissolve in the Lower Brine, and most of the Mn is diffused out of the basin [*Bignell et al*., 1976; *Gurvich*, 2006]. However, discrete layers of Mn-oxides are present in the older units (especially in CO, but also in DOP). The present study shows that Fe and Mn deposition, in fact, alternated at the scale of individual laminae, most likely because of short-term fluctuations in the chemistry of the brine pool, similar to that observed in other modern anoxic basins (e.g., Black Sea and Cariaco Basin) [*Lewis and Landing*, 1991; *Yarincik et al*., 2000], as well as in some freshwater lakes [*Davison*, 1993; *Holmström and Öhlander*, 2001].

6.2. Sulfide and Sulfate Deposition

Published fluid inclusion data from anhydrite veins close to the location of inferred venting indicate that high-temperature fluids just ~10 m below the seafloor had temperatures of at least 400°C [*Ramboz et al*., 1988; *Oudin et al*., 1984], decreasing rapidly to ~100°C in the upper sediments [e.g., *Cole*, 1988]. This cooling of the hydrothermal fluids before entering the brine pool was the main cause of sulfide precipitation in the subseafloor veins. In the current upflow zone, most of the dissolved H_2S is exhausted before the hydrothermal fluids vent into the Lower Brine, thus the amount of metal that could have been precipitated as sulfide minerals in a plume above the vent source was probably limited [*Manheim*, 1974; *Hartmann*, 1985; *Anschutz et al*., 2000; *Pierret et al*., 2001]. Because significant metal remains dissolved in the Lower Brine, any addition of H_2S causes rapid precipitation of sulfides according to their respective solubilities (Figure 19). The distribution of different sulfide phases relative to the location of the hydrothermal vents is generally consistent with the saturation states of the minerals in the Lower Brine; first chalcopyrite, and then sphalerite, dominate close to the vent sources, whereas other minerals are more common further away. Pyrite is not stable in the current brine pool [*Shanks and Bischoff*, 1977], not found in plume particles [*Hartmann*, 1973], and rare in the uppermost sediment [e.g., *Bischoff*, 1969; *Brockamp et al*., 1978], but it is abundant in some deeper units. The framboidal aggregates and local nodular texture are consistent with pyrite having formed mainly after burial [see also *Sweeney and Kaplan*, 1973].

Calcium concentrations in the pore waters are >10 times that of Red Sea deep water [*Anschutz et al*., 2000], enabling formation of anhydrite simply by heating of the sediment above ~130°C [*Blount and Dickson*, 1969]. The diffuse boundaries of the anhydrite layers and the fine disseminations observed in this study are consistent with the formation of anhydrite mainly by heating of pore fluids. The temperature increase may have been caused by fracturing associated with tectonic disturbances [*Shanks and Bischoff*, 1977], intrusion of the basaltic sill in the Southwest Basin [*Zierenberg and Shanks*, 1983], or diffusion of higher-temperature fluids into the sediments close to the vent source (indicated by clay formation temperatures higher than the temperature of the Lower Brine) [*Zierenberg and Shanks*, 1988].

6.3. Metal Enrichment of Surface-Active Particles

Zinc enrichment of Fe-(oxy)hydroxides filtered from the Lower Brine [*Hartmann*, 1973] confirms that nonferrous metals have been deposited in the sediments partly by adsorption onto surface-active particles.

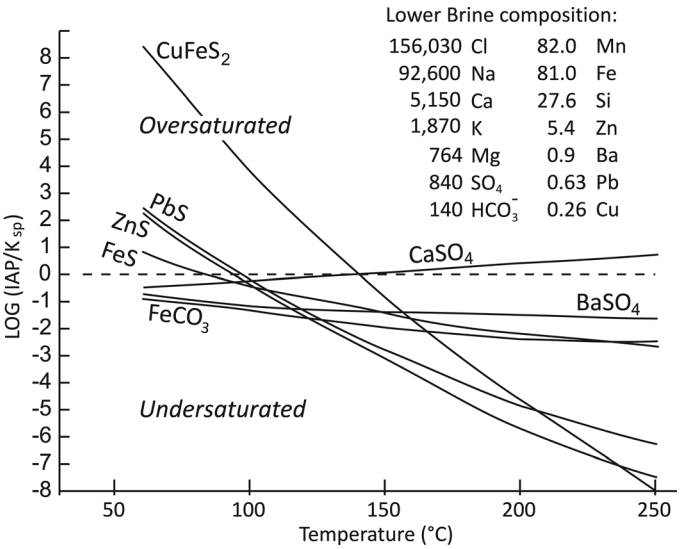

Figure 19. Saturation state of different minerals in the Lower Brine from *Shanks and Bischoff* [1977], using the brine composition of *Brewer et al.* [1965], *Miller et al.* [1966], and *Brewer and Spencer* [1969]. The Cu concentration in the Lower Brine used in this diagram (0.26 ppm Cu) is much higher than measured in 1971 (~0.03–0.12 ppm) [*Hartmann*, 1973], 1977 (~0.0005 ppm) [*Hartmann*, 1985], and 1985 (0.005 ppm) [*Anschutz et al.*, 2000]. However, the dissolved Zn concentration in the Lower Brine has remained relatively constant (2–5.3 ppm, according to the cited references). These data suggest that all Cu introduced to the Lower Brine is rapidly precipitated as chalcopyrite, whereas Zn (and Fe) remain in solution until much lower temperatures at these high salinities.

Fe-(oxy)hydroxides, or their Si-Fe-OOH precursors, have a high surface activity and likely scavenged metals as they descended through the brine pool [*Ryan et al.*, 1969; *Hartmann*, 1985; *Danielson et al.*, 1980]. In the AM unit today, metals adsorbed onto the particles are released to the uppermost sedimentary pore water following deposition, resulting in high dissolved metal concentrations in the brine-saturated sediment [*Anschutz and Blanc*, 1995b; *Anschutz et al.*, 2000]. The increase in dissolved metals in the pore waters coincides with a decrease in Si and Fe, which has been interpreted to reflect the formation of well-crystallized Si-bearing and Fe-bearing minerals with depth in the cores and release of the bound metals. Enrichment of Zn in the rims of the more crystalline Fe-oxides observed in this study is further evidence of the redistribution of metals during diagenesis.

We show that in many samples, the total amount of sulfur was far less than that needed to bind all Zn and Cu as sulfides, and in some layers, a significant proportion of the total metal has been incorporated into phases like Fe-oxides, carbonates, and clays. Most of the clays observed in our samples were amorphous or poorly crystalline and extremely fine grained, similar to the nanometer-sized clays described by *Taitel-Goldman and Singer* [2002a,b]. Very fine clays of this type are known to bind significant metals into their structures [e.g., *Hein et al.*, 1979; *Schlegel and Manceau*, 2006], and the leaching experiments confirm that clays likely played an important role in the enrichment of metals and other elements in the low-sulfur sediments.

6.4. Diagenetic and Hydrothermal Origin of Authigenic Minerals

The notable color change of the clay-rich layers from green to red-brown in some samples is similar to that observed during experimental synthesis of Fe(III) smectites by aging of Si-Fe-OOH gels [*Decarreau and Bonnin*, 1986]. In the experiments, the color change was accompanied by a decrease in pH and a drop in dissolved Si and Fe, similar to that seen in pore waters across the interface between the Lower Brine and the AM unit [*Anschutz and Blanc*, 1995b; *Anschutz et al.*, 2000]. The presence of silica infilling detrital biogenic particles and as rims around other grains observed in our study strongly suggests that silica was mobile within the sediment during diagenesis. Some of the laminae in the deeper strata also show clear evidence of hydrothermal alteration caused by intrastratal fluids, confirming an early observation by *Bischoff* [1969] and *Kaplan et al.* [1969] that detrital layers were a locus of postdepositional fluid flow and replacive mineralization. Layers from which biogenic calcite was dissolved have the highest Si contents, suggesting that the fluids responsible for calcite dissolution also deposited silica. This Si enrichment correlates with enrichment of certain trace elements (in particular Au, As, Ga, and Ba) [*Laurila et al.*, 2014a] that were likely introduced by intrastratal hydrothermal fluids rather than from the brine pool. In other layers, biogenic carbonate was replaced by manganosiderite, with strongly zoned Fe/Mn. Although Fe-carbonates and Mn-carbonates are undersaturated in the Lower Brine [e.g., *Bischoff*, 1969; *Blanc et al.*, 1998], and so are absent in AM and SU2, they are common in the lower strata, consistent with hydrothermal/diagenetic growth.

Comparison of samples from different cores shows that the fine layering changes from diffuse to well defined with depth, eventually developing sharp interfaces and clear chemical and mineralogical differences between laminae. The laminations are mostly absent in the most recently deposited brine-saturated

sediment but are present in the lower part of the AM unit, suggesting that they must have formed as a result of diagenetic recrystallization after a few meters of burial (i.e., a few thousand years). Where reduced sulfur was available (e.g., by upward diffusion from vent-proximal sources or possibly from localized bacterial sulfate reduction) [*Anschutz et al*., 2000; *Siam et al*., 2012] sulfide minerals, especially diagenetic pyrite, formed in the fluid-saturated sediment. Where pore water contained insufficient reduced sulfur to precipitate sulfides, nonsulfide metal-bearing minerals formed.

6.5. Implications for Some Ancient Ore Deposits

The Atlantis II Deep is a unique natural laboratory for understanding the formation of a number of important stratiform sedimentary ore deposits. Several models for banded iron formation (BIF) involve primary precipitation of Fe-(oxy)hydroxides, carbonates, silica, and sulfide that were then diagenetically, and later during metamorphism, transformed to more stable minerals such as chlorite, hematite, and magnetite [e.g., *Grenne and Slack*, 2003; *Klein*, 2005]. The well-known facies variations in BIF [*James*, 1954] can be compared directly to the facies variations in the Atlantis II Deep [cf. *James*, 1969; *Bischoff*, 1969]. However, the origin of millimeter-scale laminae in BIF has been the subject of considerable debate [cf. *Wang et al*., 2009; *Stefurak et al*., 2014]. Details of the primary minerals in BIF and their transformation during diagenesis and metamorphism are described by *Bekker et al*. [2010, 2013]. One model advocates differential settling of Fe-rich and Si-rich particles from the water column, possibly reflecting changes in ocean chemistry. Our study suggests that mineralogical and chemical segregation during diagenesis contributed to the fine layering of the Atlantis II sediments, a process similar to that suggested by *Lowe* [1999] and *Grenne and Slack* [2003] for banded chert.

Metal deposition from a brine pool also has been suggested as an explanation for the finely laminated ores in many volcanic-hosted and sediment-hosted base metal sulfide deposits (so-called VMS and SEDEX deposits) [*Solomon et al*., 2004; *Goodfellow and Lydon*, 2007; *Tornos et al*., 2008). The abundance of reduced sulfur (volcanic sulfur in VMS and bacteriogenic sulfide in euxinic basins that host SEDEX deposits) resulted in most metal being deposited as sulfides in those deposits, in contrast to the Atlantis II Deep. This requirement for an external source of sulfur distinguishes the Atlantis II deposit from some other large-tonnage base metal sulfide deposits [e.g., *Large et al*., 1998]. The compositional zonation of hydrothermal carbonates in the Atlantis II sediments is similar to that observed in some SEDEX deposits [e.g., *Large and McGoldrick*, 1998], and the As-rich rims on diagenetic pyrite are strikingly similar to the arsenian pyrite in a number of important sediment-hosted gold deposits (e.g., some parts of Carlin-type deposits) [*Emsbo et al*., 1999; *Large et al*., 2009]. In the Atlantis II sediments, this type of pyrite most likely formed by diagenetic growth from metal-enriched pore fluid, supporting an important model for As and Au enrichment in sediment-hosted ore deposits [*Large et al*., 2009].

Evidence of metal deposition as nonsulfide particles and the predominance of incompletely crystallized and often metastable phases in the brine pool and youngest sediments of the Atlantis II Deep also resembles models for some stratiform nonsulfide Zn deposits. *Johnson and Skinner* [2003] suggested that the nonsulfide Zn deposits at Franklin and Sterling Hill, in the New Jersey Highlands, might have formed in a manner similar to the Atlantis II sediments. But these deposits, and several other important nonsulfide Zn occurrences (e.g., parts of Broken Hill) [*Large et al*., 1996; *Huston et al*., 2006], are highly metamorphosed, raising the possibility that the original sulfides were destroyed during metamorphism.

7. Conclusions

The Atlantis II muds are chemical-clastic sediments with distinctive fine layering that is mainly diagenetic in origin. The formation of the sediments involved a number of different precipitation pathways, including mixing and cooling of hydrothermal fluids vented into the brine pool, precipitation at the chemocline, diagenetic recrystallization and hydrothermal alteration of the sediments, and subseafloor deposition. Multiple vents likely existed both in the Northeast and in the Southwest Basins, and their activity may have varied from dormant to robustly active at yearly to hundred-year time scales (similar to MOR black smoker systems) [*Hannington et al*., 2005]. Such rapid changes in the hydrothermal outflow have been confirmed from the compositions of particulate matter in the current Lower Brine [*Hartmann*, 1973, 1985]. Although precipitation directly from the brine pool was a first order control on the layering of the major sedimentary units, the present study has revealed important mineralogical differences between layer types at a much finer

scale, including possible approximate annual variations in element fluxes into the brine pool as well as diagenetic effects. Quantitative data from relogging of archived cores, detailed petrography, and sequential leaching experiments show that metals were precipitated both as sulfides and adsorbed onto surface-active particles, mainly Si-Fe-(oxy)hydroxides, that settled through the brine pool. We interpret the significant enrichment of metal in the nonsulfide components of some layers to reflect metal deposition via adsorption onto poorly crystalline Si-Fe-OOH particles, followed by incorporation in diagenetic clays and other nonsulfides after burial.

Acknowledgments

This study was funded by a CAMIRO-NSERC-CRD and a NSERC Discovery grant to M.D.H., and SEGCF Research grant to T.E.L. GEOMAR is acknowledged for making the Atlantis II sedimentary cores available for study, and Anna Krätschell and Warner Brückmann are thanked for their assistance in accessing and handling the cores. Jiri Mrazek, Judith Price, and Thor Hansteen helped with section preparation, Glenn Poirier and Mario Thöner helped with the electron beam measurements, and Renfei Feng and Darren Hunter guided the synchrotron-XRF experiments on the VESPERS beamline at the Canadian Light Source (CLS). CLS is acknowledged for granting beamtime and a travel stipendium to T.E.L. Simon Jost of University of Kiel conducted the XRF core scans of Va29-229 and Va22-275. Supporting data are included in 12 tables as part of an SI file associated with this manuscript and can also be obtained from the corresponding author (mhannington@geomar.de).

References

Anschutz, P., and G. Blanc (1993), L'histoire sédimentologique de la fosse Atlantis II (mer Rouge). Les apports de la micropaleontology, *C. R. Acad. Sci., Ser. II*, *317*, 1303–1308.

Anschutz, P., and G. Blanc (1995a), Diagenetic evolution of the DOP facies from the Atlantis II Deep (Red Sea): Evidence of early hydrothermal activity, *Oceanol. Acta*, *18*(1), 105–112.

Anschutz, P., and G. Blanc (1995b), Geochemical dynamics of the Atlantis II Deep (Red Sea): Silica behavior, *Mar. Geol.*, *128*, 25–36.

Anschutz, P., J. S. Turner, and G. Blanc (1998), The development of layering, fluxes through double-diffusive interfaces, and location of hydrothermal sources of brines in the Atlantis II Deep: Red Sea, *J. Geophys. Res.*, *103*(C12), 27,809–27819.

Anschutz, P., G. Blank, C. Monnin, and J. Boulècue (2000), Geochemical dynamics of the Atlantis II Deep (Red Sea): II. Composition of metalliferous sediment pore waters, *Geochim. Cosmochim. Acta*, *64*(23), 3995–4006.

Bäcker, H. (1976), Facies und chemische Zusammensetzung rezenter Ausfäblungen aus Mineralquellen im Roten Meer, *Geol. Jahrb.*, *D17*, 151–172.

Bäcker, H., and H. Richter (1973), Die rezente hydrothermal-seidimentärelagerstätte Atlantis II-tier im Roten Meer, *Geol. Rundsch.*, *62*, 697–740.

Badaut, D, G. Besson, A. Decarreau, and R. Rautureau (1985), Occurrence of a ferrous trioctahedral smectite in recent sediments of Atlantis II Deep, Red Sea, *Clay Miner.*, *20*, 389–404.

Badaut, D., A. Decarreau, and G. Besson (1992), Ferripyrophyllite and related Fe^{3+}-rich 2:1 clays in recent deposits of Atlantis II Deep, Red Sea, *Clay Miner.*, *27*, 227–244.

Baker E. T., J. W. Lavelle, and G. J. Massoth (1985), Hydrothermal particle plumes over the southern Juan de Fuca Ridge, *Nature*, *316*(6026), 342–344.

Basto, M. J., M. O. Figueiredo, F. Legrand, P. Chevallier, Z. Melo, and M. T. Ramos (1995), Gold assessment in micas by XRF using synchrotron radiation, *Chem. Geol.*, *124*, 83–90.

Bekker, A., J. F. Slack, N. Planavsky, B. Krapez, A. Hofmann, K. O. Konhauser, and O. J. Rouxel (2010), Iron formation: The sedimentary product of a complex interplay among mantle, tectonic, oceanic, and biospheric processes, *Econ. Geol.*, *105*, 467–508.

Bekker, A., N. Planavsky, B. Krapež, B. Rasmussen, A. Hofmann, J. F. Slack, O. J. Rouxel, and K. O. Konhauser (2013), Iron formations: Their origins and implications for ancient seawater chemistry, in *Treatise of Geochemistry*, vol. 9, edited by H. D. Holland and K. K. Turekian, pp. 561–628, Elsevier, Amsterdam, Netherlands.

Bertram, C., A. Krätschell, K. O'Brien, W. Brückmann, A. Proelss, and K. Rehdanz (2011), Metalliferous sediments in the Atlantis II Deep—Assessing the geological and economic resource potential and legal constraints, *Resour. Policy*, *36*, 315–329.

Bignell, R. D., D. S. Cronan, and J. S. Tooms (1976), Metal dispersion in the Red Sea as an aid to marine geochemical exploration, *Trans. Inst. Min. Metall., Sect. B*, *84*, 274–278.

Bischoff, J. L. (1969), Red Sea geothermal brine deposits: Their mineralogy, chemistry and genesis, in *Hot Brines and Recent Heavy Metal Deposits in the Red Sea*, edited by E. T. Degens and D. A. Ross, pp. 368–406, Springer, N. Y.

Bischoff, J. L. (1972), A ferroan nontronite from the Red Sea geothermal system, *Clays Clay Miner.*, *20*, 217–223.

Blanc, G., P. Anschutz, and M-C. Pierret (1998), Metalliferous sedimentation in the Atlantis II Deep: A geochemical insight, in *Sedimentation and Tectonics in Rift Basins: Red Sea – Gulf of Aden*, edited by B. H. Purser and W. J. Bosence Dan, pp. 505–520, Chapman and Hall, London, U. K.

Blount, C. W., and F. W. Dickson (1969), The solubility of anhydrite ($CaSO_4$) in NaCl-H_2O from 100 to 450°C and 1 to 1000 bars, *Geochim. Cosmochim. Acta*, *33*, 227–245.

Brewer, P. G., and D. W. Spencer (1969), A note on the chemical composition of the Red Sea Brines, in *Hot Brines and Recent Heavy Metal Deposits in the Red Sea*, edited by E. T. Degens and D. A. Ross, pp. 174–179, Springer, N. Y.

Brewer, P. G., J. P. Riley, and F. Culkin (1965), The chemical composition of the hot salty water from the bottom of the Red Sea, *Deep Sea Res. Oceanogr. Abstr.*, *12*, 497–503.

Brockamp, O., E. Goulart, H. Harder, and A. Heydemann (1978), Amorphous copper and zinc sulfides in the metalliferous sediments of the Red Sea, *Contrib. Mineral. Petrol.*, *68*, 85–88.

Brugger, J., A. Pring, F. Reith, C. Ryan, B. Etschmann, W. Liu, B. O'Neill, and Y. Ngothai (2010), Probing ore deposits formation: New insights and challenges from synchrotron and neutron studies, *Radiat. Phys. Chem.*, *79*, 151–161.

Butuzova, G. Y. (1984), Mineralogy and certain aspects of ore-bearing sediment genesis in the Red Sea. Part II, General processes of mineralization and ore-formation in the Atlantis II Deep, *Lithol. Miner. Resour.*, *19*(4), 293–311. [Translation from *Litologiya i Poleznye Iskopaemye*.]

Butuzova, G. Y., A. I. Gorshkov, V. A. Drits, A. A. Morozov, and A. V. Sivtsov (1988), Mineralogy and formation processes of oxidized Fe and Mn substances in the Red Sea rift zone. Part I, ore mineralogy, *Lithol. Miner. Resour.*, *23*(4), 318–329. [Translation from *Litologiya i Poleznye Iskopaemye*.]

Butuzova, G. Y., V. A. Drits, A. A. Morozov, and A. I. Gorschkov (1990), Process of formation of iron-manganese oxyhydroxides in the Atlantis-II and Thetis Deeps of the Red Sea, in *Sediment-Hosted Mineral Deposits, Int. Assoc. Sedimentol., Spec. Publ., 11*, edited by J. Parnell, Y. Lianjun, and C. Changming, pp. 57–72.

Cappuyns, V., R. Swennen, and M. Niclaes (2007), Application of the BCR sequential extraction scheme to dredged pond sediments contaminated by Pb-Zn mining: A combined geochemical and mineralogical approach, *J. Geochem. Explor.*, *93*, 78–90.

Cole, T. G. (1983), Oxygen isotope geothermometry and origin of smectite in the Atlantis II Deep, Red Sea, *Earth Planet. Sci. Lett.*, *66*, 166–176.

Cole, T. G. (1988), The nature and origin of smectite in the Atlantis II Deep, Red Sea, *Can. Mineral.*, *26*, 755–763.

Cole, T. G., and H. F. Shaw (1983a), The nature and origin of authigenic smectites in some recent marine sediments, *Clay Miner.*, *18*, 239–252.
Cole, T. G., and H. F. Shaw (1983b), Kerolite associated with anhydrite in sediments from the Atlantis II Deep, Red Sea, *Clay Miner.*, *18*, 325–331.
Cornell, R. M., R. Giovanoli, and P. W. Schindler (1987), Effect of silicate species on the transformation of ferrihydrite into goethite and hematite in alkaline media, *Clays Clay Miner.*, *35*(1), 21–28.
Craig, H. (1969), Geochemistry and origin of the Red Sea brines, in *Hot Brines and Recent Heavy Metal Deposits in the Red Sea*, edited by E. T. Degens and D. A. Ross, pp. 208–242, Springer, N. Y.
Danielson, L. G., D. Dryssen, and A. Graneli (1980), Chemical investigations of Atlantis II and Discovery brines in the Red Sea, *Geochim. Cosmochim. Acta*, *44*, 2051–2065.
Davison, W. (1993), Iron and manganese in lakes, *Earth Sci. Rev.*, *34*, 119–163.
Decarreau, A., and D. Bonnin (1986), Synthesis and crystallogenesis at low temperature of Fe(III)-smectites by evolution of coprecipitated gels: Experiments in partially reducing conditions, *Clay Miner.*, *20*, 861–877.
Degens, E. T., and D. A. Ross (1969), *Hot Brines and Recent Heavy Metal Deposits in the Red Sea*, 600 pp., Springer, N. Y.
Diem, D., and W. Stumm (1984), Is dissolved Mn^{2+} being oxidized by O_2 in absence of Mn-bacteria or surface catalyst?, *Geochim. Cosmochim. Acta*, *48*, 1571–1573.
Emsbo, P., R. W. Hutchinson, A. H. Hofstra, J. A. Volk, K. H. Bettles, G. J. Baschuk, and C. A. Johnson (1999), Syngenetic Au on the Carlin trend: Implications for Carlin-type deposits, *Geology*, *27*(1), 59–62.
Feng, R. (2005), Preliminary design report for the VESPERS beamline at the Canadian Light Source Inc., *CLS Design Note 28.2.1.2*, 58 pp., Can. Light Source Inc.
Feng, R., A. Gerson, G. Ice, R. Reininger, B. Yates, and S. McIntyre (2007), VESPERS: A beamline for combined XRF and XRD measurements, in *Synchrotron Radiation Instrumentation: Ninth International Conference, AIP Conference Proceedings*, edited by J.-Y. Choi and S. Rah, pp. 872–874, Am. Inst. of Phys, College Park, Md.
Goll, R. M. (1969), Radiolaria: The history of a brief invasion, in *Hot Brines and Recent Heavy Metal Deposits in the Red Sea*, edited by E. T. Degens and D. A. Ross, pp. 306–312, Springer, N. Y.
Goodfellow, W. D., and J. W. Lydon (2007), Sedimentary exhalative (SEDEX) deposits, in *Mineral deposits of Canada: A synthesis of Major Deposit Types, District Metallogeny, the Evolution of Geological Provinces, and Exploration Methods*, edited by W. D. Goodfellow, *Geol. Assoc. Can. Spec. Publ., 5*, pp. 163–183.
Goulart, E. P. (1976), Different smectite types in sediments of the Red Sea, *Geol. Jahrb.*, *D17*, 135–149.
Grenne, T., and J. F. Slack (2003), Bedded jaspers of the Ordovician Løkken ophiolite, Norway: Seafloor deposition and diagenetic maturation of hydrothermal plume-derived silica-iron gels, *Miner. Deposita*, *38*, 625–639.
Guney, M., M. A. Al-Marhoun, and Z. A. Nawab (1988), Metalliferous sub-marine sediments of the Atlantis-II-Deep, Red Sea, *CIM Bull.*, *81*, 33–39.
Gurvich, E. G. (2006), *Metalliferous Sediments of the World Ocean: Fundamental Theory of Deep-Sea Hydrothermal Sedimentation*, 423 pp., Springer, Heidelberg, Germany.
Hackett, J. P., and J. L. Bischoff (1973), New data on the stratigraphy, extent, and geologic history of the Red Sea geothermal deposits, *Econ. Geol.*, *68*, 553–564.
Hall, G. E. M., J. E. Vaive, R. Beer, and M. Hoashi (1996), Selective leaches revisited, with emphasis on the amorphous Fe oxyhydroxides phase extraction, *J. Geochem. Explor.*, *56*, 59–78.
Hannington, M. D., C. E. J. de Ronde, and S. Petersen (2005), Modern sea-floor tectonics and submarine hydrothermal systems, in *100th Anniversary Volume of Economic Geology*, edited by J. F. Hedenquist et al., pp. 111–142, Society of Economic Geologists, Littleton, Colo.
Hartmann, M. (1973), Untersuchungen von suspendiertem Material in den Hydrothermallaugen des Atlantis-II-Tiefs, *Geol. Rundsch.*, *62*, 742–754.
Hartmann, M. (1985), Atlantis-II-Deep geothermal brine system: Chemical processes between hydrothermal brines and Red Sea deep water, *Mar. Geol.*, *64*, 157–177.
Hein, J. R., C. R. Ross, and H. Yeh (1979), Mineralogy and diagenesis of surface sediments from Domes area A, B and C, in *Marine Geology and Oceanography of the Pacific Manganese Nodule Province*, edited by J. L. Bischoff and D. Z. Piper, pp. 365–396, Plenum, N. Y.
Hendricks, R. L., F. B. Reisbick, E. J. Mahaffey, D. B. Roberts, and M. N. A. Peterson (1969), Chemical composition of sediments and interstitial brines from the Atlantis II, Discovery and Chain Deeps, in *Hot Brines and Recent Heavy Metal Deposits in the Red Sea*, edited by E. T. Degens and D. A. Ross, pp. 407–440, Springer, N. Y.
Hlavay, J., T. Prohaska, M. Weisz, W. W. Wenzel, and G. J. Stingeder (2004), Determination of trace elements bound to soils and sediment fractions [IUPAC Technical Report], *Pure Appl. Chem.*, *76*(2), 415–442.
Holm, N. G., M. J. Dowler, T. Wadsten, and G. Arrhenius (1983), β-FeOOH·Cl_n (akaganéite) and $Fe_{1-x}O$ (wüstite) in hot brine from the Atlantis II Deep (Red Sea) and the uptake of amino acids by synthetic β-FeOOH·Cl_n, *Geochim. Cosmochim. Acta*, *47*, 1465–1470.
Holmström, H., and B. Öhlander (2001), Layers rich in Fe- and Mn-oxyhydroxides formed at the tailings-pond water interface, a possible trap for trace metals in flooded mine tailings, *J. Geochem. Explor.*, *74*, 189–203.
Huston, D. L., B. Stevens, P. N. Southgate, P. Muhling, and L. Wyborn (2006), Australian Zn-Pb-Ag ore-forming systems: A review and analysis, *Econ. Geol.*, *101*, 1117–1157.
James, H. L. (1954), Sedimentary facies of iron-formation, *Econ. Geol.*, *49*, 235–293.
James, H. L. (1969), Comparison between Red Sea deposits and older ironstone and iron-formation, in *Hot Brines and Recent Heavy Metal Deposits in the Red Sea*, edited by E. T. Degens and D. A. Ross, pp. 525–532, Springer, N. Y.
Johnson, C. A., and B. J. Skinner (2003), Geochemistry of the Furnace magnetite bed, Franklin, New Jersey, and the relationship between stratiform iron oxide ores and stratiform zinc oxide-silicate ores in the New Jersey Highlands, *Econ. Geol.*, *98*, 837–854.
Kaplan, I. R., R. E. Sweeney, and A. Nissenbaum (1969), Sulfur isotope studies on Red Sea geothermal brines and sediments, in *Hot Brines and Recent Heavy Metal Deposits in the Red Sea*, edited by E. T. Degens and D. A. Ross, pp. 474–498, Springer, N. Y.
Klein, C. (2005), Some Precambrian banded iron-formations (BIFs) from around the world: Their age, geologic setting, mineralogy, metamorphism, geochemistry, and origin, *Am. Mineral.*, *90*, 1473–1499.
Knedler, K. E. (1985), A geochemical and ^{57}Fe Mossbauer investigation of East Pacific Rise and the Red Sea metalliferous sediments and other selected marine sedimentary deposits, PhD thesis, Victoria Univ. of Wellington, New Zealand.
Ku, T. L., D. L. Thurber, and G. G. Mathieu (1969), Radiocarbon chronology of Red Sea sediments, in *Hot Brines and Recent Heavy Metal Deposits in the Red Sea*, edited by E. T. Degens and D. A. Ross, pp. 348–359, Springer, N. Y.

Large, R. R., and P. J. McGoldrick (1998), Lithogeochemical halos and geochemical vectors to stratiform sediment hosted Zn-Pb-Ag deposits, 1. Lady Loretta Deposit, Queensland, *J. Geochem. Explor.*, *63*, 37–56.
Large, R. R., S. Bodon, G. J. Davidson, and D. Cooke (1996), The chemistry of BHT ore formation—One of the keys to understanding the difference between SEDEX and BHT deposits, in *Proceedings of a Workshop on New Developments in Broken Hill Type Deposits, CODES*, edited by J. Pongratz and G. J. Davidson, pp. 105–111, Univ. of Tasmania, Australia.
Large, R. R., S. W. Bull, D. R. Cooke, and P. J. McGoldrick (1998), A genetic model for the H.Y.C. Deposit, Australia; based on regional sedimentology, geochemistry, and sulfide-sediment relationships, *Econ. Geol.*, *93*, 1345–1368.
Large, R. R., et al. (2009), Gold and trace element zonation in pyrite using a laser imaging technique: Implications for the timing of gold in orogenic and Carlin-style sediment-hosted deposits, *Econ. Geol.*, *104*, 635–668.
Laurila, T. E., M. D. Hannington, S. Petersen, and D. Garbe-Schönberg (2014a), Trace metal distribution in the Atlantis II Deep (Red Sea) sediments, *Chem. Geol.*, *386*, 80–100.
Laurila, T. E., M. D. Hannington, S. Petersen, and D. Garbe-Schönberg (2014b), Early depositional history of metalliferous sediments in the Atlantis II Deep of the Red Sea: Evidence from rare earth element geochemistry, *Geochim. Cosmochim. Acta*, *126*, 146–168.
Lewis, B. L., and W. M. Landing (1991), The biogeochemistry of manganese and iron in the Black Sea, *Deep Sea Res., Part A*, *38*(2), 5773−5803.
Lowe, D. R. (1999), Petrology and sedimentology of cherts and related silicified sedimentary rocks in the Swaziland Supergroup, in *Geologic Evolution of the Barberton Greenstone Belt, South Africa*, edited by D. R. Lowe and G. R. Byerly, *Geol. Soc. Am. Spec. Pap.*, *329*, pp. 83–114.
Manheim, F. T. (1974), Red Sea geochemistry, in *Initial Reports of the Deep Sea Drilling Project*, vol. 23, edited by R. B. Whitmarsh et al., chap. 38, pp. 975–998, U.S. Gov. Print. Off., Washington, D. C.
Miller, A. R. (1964), Highest salinity in the world ocean?, *Nature*, *203*, 590.
Miller, A. R., D. C. Densmore, E. T. Degens, J. C. Hathaway, F. T. Manheim, P. F. McFarlin, R. Pocklington, and A. Jokela (1966), Hot brines and recent iron deposits in deeps of the Red Sea, *Geochim. Cosmochim. Acta*, *30*, 341–359.
Missack, E., P. Stoffers, and A. El Goresy (1989), Mineralogy, parageneses, and phase relations of copper-iron sulfides in the Atlantis II Deep, Red Sea, *Miner. Deposita*, *24*, 82–91.
Nawab, Z. A. (1984), Red Sea mining: A new era, *Deep Sea Res., Part A*, *31*, 813–822.
Oudin, E., Y. Thisse, and C. Ramboz (1984), Fluid inclusion and mineralogical evidence for high temperature saline hydrothermal circulation in the Red Sea metalliferous sediments: Preliminary results, *Mar. Min.*, *5*(1), 3–31.
Pierret, M. C., N. Clauer, D. Bosch, G. Blanc, and C. France-Lanord (2001), Chemical and isotopic ($^{87}Sr/^{86}Sr$, $\delta^{18}O$, δD) constraints to the formation processes of Red-Sea brines, *Geochim. Cosmochim. Acta*, *65*(8), 1259–1275.
Pottorf, R. J., and H. L. Barnes (1983), Mineralogy, geochemistry, and ore genesis of hydrothermal sediments from the Atlantis II Deep, Red Sea, *Econ. Geol. Monogr.*, *5*, 198–223.
Ramboz, C., E. Oudin, and Y. Thisse (1988), Geyser-type discharge in Atlantis II Deep, Red Sea: Evidence of boiling from fluid inclusions in epigenetic anhydrite, *Can. Mineral.*, *26*, 765–786.
Ryan, W. B. F., E. M. Thorndic, M. Ewing, and D. A. Ross (1969), Suspended matter in the Red Sea brines and its detection by light scattering, in *Hot Brines and Recent Heavy Metal Deposits in the Red Sea*, edited by E. T. Degens and D. A. Ross, pp. 153–157, Springer, N. Y.
Schlegel, M. L., and A. Manceau (2006), Evidence for the nucleation and epitaxial growth of Zn phyllosilicate on montmorillonite, *Geochim. Cosmochim. Acta*, *70*, 901–917.
Schoell, M. (1976), Heating and convection within the Atlantis II Deep geothermal system of the Red Sea, in *Proceeding of Second United Nations Symposium on the Development and Use of Geothermal Resources*, vol. 1, 583–590, U.S. Energy Research and Development Administration, U.S. Govern. Print. Off., Washington, D. C.
Schoell, M., and W. Stahl (1972), The carbon isotopic composition and the concentration of dissolved anorganic carbon in the Atlantis II Deep brines/Res Sea, *Earth Planet. Sci. Lett.*, *15*, 206–211.
Schwertmann, U., and R. M. Cornell (2000), *Iron Oxides in the Laboratory: Preparation and Characterization*, 2nd ed., Wiley-VCH Verl. GmbH, Weinheim, Germany.
Schwertmann, U., and E. Murad (1983), Effect of pH on the formation of goethite and hematite from ferrihydrite, *Clays Clay Miner.*, *31*(4), 277–284.
Schwertmann, U., J. Friedl, H. Stanjek, E. Murad, and C. Bender Koch (1998), Iron oxides and smectites in sediments from the Atlantis II Deep, Red Sea, *Eur. J. Mineral.*, *10*, 953–967.
Shanks, W. C., and J. L. Bischoff (1977), Ore transport and deposition in the Red Sea geothermal system: A geochemical model, *Geochim. Cosmochim. Acta*, *41*, 1507–1519.
Shanks, W. C., and J. L. Bischoff (1980), Geochemistry, sulfur isotope composition and accumulation rates of Red Sea geothermal deposits, *Econ. Geol.*, *75*, 445–459.
Siam, R., et al. (2012), Unique prokaryotic consortia in geochemically distinct sediments from Red Sea Atlantis II and Discovery Deep brine pools, *PLoS ONE*, *7*(8), e42872.
Singer, A., and P. Stoffers (1981), Hydrothermal vermiculite from the Atlantis II Deep, Red Sea, *Clays Clay Miner.*, *29*(6), 454–458.
Singer, A., and P. Stoffers (1987), Mineralogy of a hydrothermal sequence in a core from the Atlantis II Deep, Red Sea, *Clay Miner.*, *22*, 251–267.
Solomon, M., F. Tornos, R. R. Large, J. N. P. Badham, R. A. Both, and K. Zaw (2004), Zn-Pb-Cu volcanic-hosted massive sulphide deposits: Criteria for distinguishing brine pool-type from black smoker-type sulphide deposition, *Ore Geol. Rev.*, *25*, 259–283.
Stefurak, E. J. T., D. R. Lowe, D. Zentner, and W. W. Fischer (2014), Primary silica granules—A new mode of Paleoarchean sedimentation, *Geology*, *42*(4), 283–286.
Stephens, J. D., and R. W. Wittkopp (1969), Microscopic and electron beam microprobe study of sulfide minerals in Red Sea mud samples, in *Hot Brines and Recent Heavy Metal Deposits in the Red Sea*, edited by E. T. Degens and D. A. Ross, pp. 441–447, Springer, N. Y.
Stoffers, P., and D. A. Ross (1974), Sedimentary history of the Red Sea, in *Initial Reports of the Deep Sea Drilling Project*, vol. 23, edited by R. B. Whitmarsh et al., chap. 23, pp. 849–865, U.S. Gov. Print. Off., Washington, D. C.
Sval'nov V. N., V. P. Strizhov, Y. A. Bogdanov, and A. B. Isayeva (1984), Hydrothermal barite crust on basalts in the Atlantis II Deep (Red Sea), *Oceanology*, *24*(6), 716–720.
Sweeney, R. E., and I. R. Kaplan (1973), Pyrite framboid formation: Laboratory synthesis and marine sediments, *Econ. Geol.*, *68*(5), 618–634.
Swift, A., A. S. Bower, and R. Schmitt (2012), Vertical, horizontal, and temporal changes in temperature in the Atlantis II and Discovery hot brine pools, Red Sea, *Deep Sea Res., Part I*, *64*, 118–128.
Taitel-Goldman, N., and A. Singer (2001), High-resolution transmission electron microscopy study of newly formed sediments in the Atlantis II Deep, Red Sea, *Clays Clay Miner.*, *49*(2), 174–182.

Taitel-Goldman, N., and A. Singer (2002a), Metastable Si-Fe phases in hydrothermal sediments of Atlantis II Deep, Red Sea, *Clay Miner.*, *37*, 235–248.

Taitel-Goldman, N., and A. Singer (2002b), Synthesis of clay-sized iron oxides under marine hydrothermal conditions, *Clay Miner.*, *37*, 719–731.

Taitel-Goldman, N., C. B. Koch, and A. Singer (2002), Lepidocrocite in hydrothermal sediments of the Atlantis II and Thetis Deeps, Red Sea, *Clays Clay Miner.*, *50*(2), 186–197.

Taitel-Goldman, N., C. B. Koch, and A. Singer (2004), Si-associated goethite in hydrothermal sediments of the Atlantis II and Thetis Deeps, Red Sea, *Clays Clay Miner.*, *52*(1), 115–129.

Taylor, S. R., and S. M. McLennan (1985), *The Continental Crust: Its Composition and Evolution*, Blackwell, Oxford, U. K.

Tessier, A., P. G. C. Campbell, and M. Blsson (1979), Sequential extraction procedure for the speciation of particulate trace metals, *Anal. Chem.*, *51*(7), 844–851.

Tornos, F., M. Solomon, C. Conde, and B. Spiro (2008), The formation of the Tharsis massive sulfide deposit, Iberian Pyrite Belt: Geological, lithogeochemical, and stable isotope evidence for deposition in a brine pool, *Econ. Geol.*, *103*, 185–214.

Wang, Y., H. Xu, E. Merino, and H. Konishi (2009), Generation of banded iron formations by internal dynamics and leaching of oceanic crust, *Nat. Geosci.*, *2*, 781–784.

Weber-Diefenbach, K. (1977), Geochemistry and diagenesis of recent heavy metal ore deposits at the Atlantis II Deep (Red Sea), in *Time and Strata-bound Ore Deposits*, edited by D. D. Klemm and H. J. Schneider, pp. 419–436, Springer, Berlin.

Yarincik, K. M., R. W. Murray, T. W. Lyons, L. C. Peterson, and G. H. Haug (2000), Oxygenation history of bottom waters in the Cariaco Basin, Venezuela, over the past 578,000 years: Results from redox-sensitive metals (Mo, V, Mn, and Fe), *Paleoceanography*, *15*(5), 593–604.

Zierenberg, R. A., and W. C. Shanks (1983), Mineralogy and geochemistry of epigenetic features in metalliferous sediments, Atlantis II Deep, Red Sea, *Econ. Geol.*, *78*, 57–72.

Zierenberg, R. A., and W. C. Shanks (1988), Isotopic studies of epigenetic features in metalliferous sediment, Atlantis II Deep, Red Sea, *Can. Mineral.*, *26*, 737–753.